



POLITECNICO MILANO 1863

School of Industrial and Information
Engineering

“Synthesis and Characterization of Colloidal Antimony SulfoBromide (SbSBr) Nanocrystals”.

Laurea Magistrale in **Materials Engineering and Nanotechnology**.

Under the Supervision of:

External Supervisor;

Dr. Carlo Giansante, (Researcher, CNR-Nanotec, Lecce, Italy.)

Internal Supervisor;

Prof. Dr. Pierangelo Metrangolo, (Prof., Polimi, Milano, Italy.)

Student

Mr. Sravan Erkulla – 944307.

A.Y 2022-2023

Acknowledgement:

I like to take this opportunity to thank the people who were involved during the execution and evaluation part of this thesis work. I strongly believe that the words framed here may be less to express the gratitude towards them.

Firstly, I would like to thank my supervisor **Dr. Carlo Giansante** (Researcher-CNR Nanotec), for the guidance, valuable suggestions and the eternal support which he had provided during the execution part of this thesis work. It was a great pleasure of mine to be the student of **Dr. Carlo Giansante**, this thesis wouldn't been possible without his immense support.

I sincerely thank to my academic supervisor **Prof. Dr. Pierangelo Metrangolo** (Polimi), for accepting me as a thesis student under him, and by providing me with an adequate support during my thesis work at CNR-Nanotec, lecce.

I am very much thankful to **Dr. David Maria Tobaldi**, for teaching me XRD analysis from the scratch and thankyou very much for introducing me GSAS-II for refinement and for providing me all the sources to learn it.

I also like to show my gratitude by thanking to **Dr. Nobile Concetta**, for teaching me TEM analysis from the basics to advance.

I am thankful to **Mr. Diego Mangiullo**, for the support he had provided to my thesis work by providing the lab-requirements in order to execute the works at CNR-Nanotec by time.

I feel this might be less to express, I am grateful and thankful to be the student of CNR-Nanotec, Nano chemistry lab which is headed by **Dr. Luigi Carbone**, for the support he had provided in both of the ways personally and academically.

I am also thankful to **Dr. Riccardo Scarfiello**, **Dr. Alessandra Quarta**, and **Dr. Clara Piccirillo**, for their constant support and help in the lab during the experimental works in the lab.

I also like to thank my friends at CNR-Nanotec, for making me comfortable and by providing me with the required help in need.

Abstract:

In the current thesis work, I present a colloidal approach for the synthesis of antimony sulfobromide nanocrystals (SbSBr NCs). Through this method I have obtained a pure phase material, i.e., an orthorhombic crystal structure elongated along the c crystallographic axis. The SbSBr NCs have revealed concentration-dependent properties by varying the band-gap in the visible spectral range with an effective absorption coefficient value. The SbSBr NCs show chemical stability at standard laboratory conditions without undergoing any phase change.

The results obtained by the reported method, i.e., synthesizing SbSBr NCs in colloidal form, may pave the way to non-toxic and abundantly available materials for applications in the field of energy conversion.

Keywords: Antimony sulfobromide-SbSBr; Colloidal nanocrystals (NCs); Surface chemistry; Photo-physics.

Summario:

Nel presente lavoro di tesi, presento un approccio colloidale per la sintesi di nanocristalli di solfobromuro di antimonio (SbSBr NC). Attraverso questo metodo ho ottenuto un materiale in fase pura, cioè una struttura cristallina ortorombica allungata lungo l'asse cristallografico c. I NC SbSBr hanno rivelato proprietà dipendenti dalla concentrazione variando il band-gap nell'intervallo spettrale del visibile con un valore di coefficiente di assorbimento efficace. I NC SbSBr mostrano stabilità chimica alle condizioni standard di laboratorio senza subire alcun cambiamento di fase.

I risultati ottenuti con il metodo riportato, ovvero la sintesi di NC SbSBr in forma colloidale, possono aprire la strada a materiali non tossici e abbondantemente disponibili per applicazioni nel campo della conversione energetica.

Parole chiave: Sulfobromuro di antimonio-SbSBr; Nanocristalli colloidali (NCs); Chimica delle superfici; Fotofisica.

Table of Contents:

- I. Acknowledgement.
- II. Abstract.
- III. Summario.
- IV. List of Figures.
- V. List of Tables.
- VI. List of Abbreviations.

1. Introduction.	1-6
1.1. About colloidal nanocrystals.	
1.2. State-of-the-art.	
1.3. Research issue.	
1.4. Aim of the Thesis.	
1.5. Outline of the Thesis.	
2. Physics involved in colloidal semiconductor nanocrystals.	7-14
2.1. General physics of colloidal semiconductor NCs.	
2.2. Quantum size effects.	
2.2.1. Particle in a sphere.	
2.3. Practical evidence for quantum confinement.	
2.3.1. Absorption spectrum.	
2.3.2. Photoluminescence and strokes shift.	
3. Chemistry involved in the colloidal semiconductor nanocrystals.	15-23
3.1. Introduction.	
3.2. Synthesis of colloidal semiconductor nanocrystals.	
3.2.1. Hot-injection synthesis of semiconductor nanocrystals.	
3.2.1.1. LaMer and Ostwald Theories.	
3.3. Classical theories of nucleation and growth of nanocrystals in solution.	
3.3.1. Homogeneous and Heterogeneous nucleation of nanocrystals.	
3.4. Size and Shape control of nanocrystal.	
3.5. Ligand replacement.	
3.5.1. Solution phase ligand exchange.	
3.5.2. Solid state ligand exchange.	
4. Characterization methods.	24-34
4.1. Morphological characterization- TEM and SEM.	
4.2. Structural characterization – X-ray diffraction spectroscopy (XRD).	
4.3. Compositional characterization.	
4.3.1. Inductively coupled plasma atomic emission spectroscopy – (ICP-AES).	
4.4. Surface chemistry.	

- 4.4.1. Fourier-transformed infrared spectroscopy (FTIR).
- 4.4.2. Nuclear magnetic resonance spectroscopy (NMR).
- 4.5. Optical characterization – UV-Visible & NIR spectroscopy and Photoluminescence-spectroscopy.

5. Synthesis of colloidal SbSBr nanocrystals. 35-59

- 5.1. Materials.
- 5.2. Synthesis Procedure.
 - 5.2.1. Optimization of Parameters.
 - 5.2.1.1. Optimization of reagents concentration.
 - a. Case 1.
 - b. Case 2.
 - 5.2.1.2. Optimization of the reaction Time.
- 5.3. Results and Discussion.
 - 5.3.1. Morphological, Structural, and Optical Characterization.
 - a. Morphological analysis.
 - b. Structural analysis.
 - c. Optical analysis.
 - d. Theoretical analysis.
 - e. Stability and surface chemistry of SbSBr NCs.

6. Conclusion. 60

7. References. 61-66

List of Figures.

- Fig. 2. 1. Schematic representation of the band structure of the bulk crystals, which depicts the continuous energy levels¹. 8
- Fig. 2. 2. Schematic observation of the effect of quantum confinement on the electronic structure of semiconductor material². 8
- Fig. 2. 3. Schematic view of the edge-on-edge and diagonal edge-on-edge transition of semiconductor material³. 11
- Fig. 2. 4. a. Schematic observation of the CdSe NCs at room temperature absorption spectrum. b. Electronic spectrum of CdS at varied size³. 12
- Fig. 2. 5. a. Schematic observation of the allowed inter-band transitions in CdSe. b. CdSe absorption spectrum with the well resolved transitions³. 13
- Fig. 3. 1. Schematic representation of the LaMer theory of nucleation and growth mechanism w.r.t to the concentration of the monomers vs time⁴. 17
- Fig. 3. 2. Schematic representation of the nanocrystal size dependence on the monomer concentration and its growth rate⁴. 20
- Fig. 4. 1. Schematic representation of the signals generated during the interaction of highly energized electron beam when subjected onto the sample⁵. 24
- Fig. 4. 2. Optic ray diagram for obtaining a) bright field, b) dark field c) High resolution imaging in TEM, and d) sample imaging in TEM. 26
- Fig. 4. 3. Bragg diffraction from a crystal with inter atomic spacing 'd'⁶. 29
- Fig. 5. 1. a, b, and c are the images of as-synthesized SbSBr NCs. 43
- Fig. 5. 2. d, e, f, and g, are TEM images of as-synthesized 0.4-SbSBr-180°C NCs. 45
- Fig. 5. 3. h, i, j, and k, are TEM images of as-synthesized 0.5-SbSBr-180°C NCs. 46
- Fig. 5. 4. l, m, n, and o, are TEM images of as-synthesized 0.5-SbSBr-150°C NCs. 47
- Fig. 5. 5. Refinement fit obtained on the data obtained with 0.4mmol Sb(Ac)3 conc. at 180°C⁷. 48
- Fig. 5. 6. Refinement fit obtained on the data obtained with 0.5mmol Sb(Ac)3 conc. at 180°C⁷. 49
- Fig. 5. 7. Refinement fit obtained on the data obtained with 0.5mmol Sb(Ac)3 conc. at 150°C⁷. 50
- Fig. 5. 8. Post refinement, computed crystallographic data obtained on 0.5mmol Sb(Ac)3 conc. at 180°C, Sb-pink, S-yellow, and Br-brown⁸. 51
- Fig. 5. 9. The offset intensity patterns of XPD data of 0.5-SbSBr at 180°C, 0.4-SbSBr at 180°C, 0.5-SbSBr at 150°C, 0.5-SbSBr at 130°C, and Sb₂S₃ NCs at 180°C^{9,10}. 52
- Fig. 5. 10. XRD pattern of 0.5-SbSBr at 180°C with the cross reference of 00-231-0798^{9,10}. 53
- Fig. 5. 11. XRD pattern of 0.4-SbSBr at 180°C with the cross reference of 00-231-0798^{9,10}. 53
- Fig. 5. 12. XRD pattern of 0.5-SbSBr at 150°C with the cross reference of 00-231-0798^{9,10}. 54
- Fig. 5.13. Absorbance of 0.5-SbSBr at 180°C with band gap using the Tauc plot⁹. 55

- *Fig. 5. 14. Tauc plot for indirect transitions for 0.5-SbSBr at 180°C.* 55
- *Fig. 5. 15. Tauc plot for direct transitions for 0.5-SbSBr at 180°C.* 56
- *Fig. 5. 16. Absorbance of 0.4-SbSBr at 180°C with band gap using the Tauc plot⁹.* 56
- *Fig. 5.17. Absorbance of 0.5-SbSBr at 150°C with band gap using the Tauc plot⁹.* 57
- *Fig. 5.18. Computed band gap structure and density of states of SbSBr, along with the PDOS^{9,10}.* 58
- *Fig. 5.19. Computed energy levels of atomic orbitals of 0.5-SbSBr at 180°C.* 58
- *Fig. 5.20. FTIR spectra of 0.5-SbSBr NCs at 180°C, capped with oleic acid.* 59

List of Tables.

- *Table. 5. 1. Colour transition Observation with 0.15 mmol of Sb(Ac)3 @180°C.* 36
- *Table. 5. 2. Colour transition Observation with 0.4 mmol of Sb(Ac)3 @180°C.* 38
- *Table. 5. 3. Colour transition Observation with 0.4 mmol of Sb(Ac)3 @150°C.* 39
- *Table. 5. 4. Colour transition Observation with 0.4 mmol of Sb(Ac)3 @230°C.* 39
- *Table. 5. 5. Colour transition Observation with 0.5 mmol of Sb(Ac)3 @180°C.* 40
- *Table. 5. 6. Colour transition Observation with 0.5 mmol of Sb(Ac)3 @150°C.* 41
- *Table. 5. 7. Colour transition Observation with 0.5 mmol of Sb(Ac)3 @230°C.* 41
- *Table. 5. 8. Colour transition Observation with 0.6 mmol of Sb(Ac)3 @180°C.* 42
- *Table. 5. 9. Colour transition Observation with 0.5 mmol of Sb(Ac)3 @180°C- 15min.* 43
- *Table. 5. 10. Observation of the variation obtained in the synthesized 0.5-SbSBr-180°C lattice parameters.* 49

List of Abbreviations.

Abs.	Absorption.
CdTe	Cadmium Telluride.
CIGS	Copper Indium Gallium Selenide.
Conc.	Concentration.
Cs	Caesium.
CZTSSe	Copper Zinc Tin Sulphur Sellenide.
EDX	Energy Dispersed X-ray Spectroscopy.
E_g	Band Gap.
Fig.	Figure.
FTIR	Fourier Transform Infrared spectroscopy.
Ge	Germanium.
NCs	Nanocrystals.
nm	Nanometer.
Pb	Lead.
PL	Photoluminescence.
PLQY	Photoluminescence Quantum Yield.
QDs	Quantum Dots.
RT	Reaction Temperature.
SAD	Selective Area Diffraction.
SbSBr	Antimony SulfoBromide.
SEM	Scanning Electron Microscopy.
Sn	Stannum (Tin).
Sol'n	Solution.
TEM	Transmission Electron Microscopy.
UV	Ultraviolet Spectrum.
Vis.	Visible Spectrum.
XRD	X-ray Diffraction Spectroscopy.

1. Introduction.

1.1. About colloidal nanocrystals.

Colloidal inorganic nanocrystals are among the most intriguing areas of research, in the domain of nanoscience and nanotechnology. They are relevant to the size-dependent properties of the (nano)materials and the bottom-up approach for the development of functional materials and their devices. The major aspects which rise the admittance of colloidal nanocrystals are: a significant conc. of the ligands on the surface of nanocrystals which leads to a large surface-to-volume ratio of the nanocrystals (NCs) and the confinement of the charge carrier motion to particular volume^{11–21}. At the nano-size scale, the following aspects affect the properties of the particles: surface and strain-driven lattice distortions, and varied density of states, which evolves systematically and exhibits an impact on the structural stability and magneto-opto-electrical responses^{22–25}.

In addition, quantum confinement is said to be attained by a particle, when a limiting threshold size is reached, which leads to the widening of the band gap and level spacing at near band edges. When we opt for a restrictive decrease in the dimension parameter of a material, below its electron mean free path, an intense absorption of photons arises. Furthermore, the constrained size of the electronic structure of the NCs, provides a tool to alter the dynamics of the red-ox process, which enables for the unusual structural remodification at their surface, conferring the possibilities of catalytic properties^{26–34}. It is worth mentioning, that nanoparticles of magnetic and electric materials can behave as single domains and their properties can be influenced by thermal fluctuations, which rely on the particle size and its surface defects, a quite contrasting comparison can be observed from bulk materials to nanoparticles^{35–37}. Concerning the aforementioned conditions, nanoparticles can be utilized in an exceptionally wide range of applications, from which the fundamental to the advanced level of an area of interest can be approached. To the end, if we consider the diverse range of applications which include, energy generation to biomedicine, the commercialization of nanocrystal-based devices is on its their way toward the reach of every individual and they are already in existence^{17–21,29,30,38–41} in some particular applications. A short brief on semiconductor nanocrystals is provided next to this portion of the chapter.

1.2. State-of-the-art.

Synthesis of nanoparticles is an extremely active area of research in material science, for the development of unprecedented functional materials. Major consequences, which were faced during the synthesis of nanocrystals are the control over chemical composition, size, and shape. Over the past 6 decades, silicon and germanium were the only elemental semiconductor materials that have been positioned as efficient and cost-effective photovoltaics (PV)⁴²⁻⁴⁴. Further, opportunities for compound semiconductor materials have raised, with the introduction of the thin film technique in the electronics sector⁴⁵⁻⁴⁷, such as CdTe^{48,49}, Cu(InGe)Se₂ (CIGS)^{50,51}, Cu₂ZnSn(S, Se)₄ (CZTSSe)^{50,52-54} and organic semiconductor materials⁴⁷. These materials efficiently harvest a large portion of the solar spectrum, by constructing tandem or multijunction devices, through which they execute higher efficiency than the Shockley-Queisser limit of a single junction cell⁵². However, the commercialized devices based on CdTe and CIGS, suffer from the scarcity of Te and In, for the further deployment of large-scale energy production, which led the researchers to look for the counterpart CZTSSe, which includes earth-abundant and non/less toxic substance⁵⁵. The synthesis of CZTSSe compound requires a high temperature of >500°C, some lattice instabilities, and multi-phase formation during the synthesis, which limits the advancement of the aforementioned compound for commercialization^{50,55,56}.

In recent times ternary halide-based compounds, such as Pb halide perovskites, had emerged as a promising substitution for old silicon-based PV's, with high performing efficiencies of 25.8%^{57,58}. In contrast, the highly efficient compounds are majorly composed of lead (Pb), which entails the toxicity issue during the fabrication to the disposal period. As Pb-based compounds undergo, a rapid degradation on exposure to external entities (such as moisture, heat, and illumination, etc.) due to the above challenges, Pb-based compounds are exposed to restrictions for commercialization⁵⁹⁻⁶². Besides the challenges, moreover, the instability of Pb-halide perovskites motivated the researchers, to search for an alternative element, which could replace Pb, with near similarities in optoelectric and ferroelectric properties^{59,63,64}. To this regard, Sn²⁺ and Ge²⁺ was identified as suitable replacements for Pb, which fulfil the following conditions, ionic radii, coordination, and charge which balances the requirement for perovskite structure⁶⁵⁻⁷². As Sn²⁺ and Ge²⁺ cations in perovskite structure can be easily oxidized to Sn⁴⁺ and Ge⁴⁺, which provokes instability, degradation, and low-performance conditions and makes the aforementioned halide-based perovskites,

as unsuitable compounds for the energy harvesting process, compared to Pb-based perovskites^{73–76}. An effective photo absorption of the solar spectrum is also achieved by chalcogenides and double perovskites⁷⁷ of transition metal elements, whose structure is depicted as $A_3B_2Q_9$ ^{77,78}(3:2). Chalcogenides-based compounds are a prominent group, which exhibit better physico-chemical properties and stability in harsh environments, over the halide-based compounds for photovoltaic applications. Nevertheless, in transition metal chalcogenides, band gap, absorption coefficient, and optical properties can be tailored by replacing with other chalcogenide elements which possess higher ionic radius (S or Se or Te) or by using mixed chalcogenides ($ABQ_{1-x}Q_x$)^{78–81}. As halide-based perovskites with a narrow band gap, are highly efficient compounds with structural instability, which arises due to the high electronegativity of X and ionic bond character between, edge-sharing element (X) and corner-sharing tetrahedral sites (B-X) which makes these compounds unstable. Overall, to the above in search of a suitable material for charge conversion and transport approaches, researchers have found other semiconductor families, which include Chalcopyrites^{78,80–83}, Kesterites⁸⁴ and Chalcohalides^{85,86}.

However, to overcome the criticalities of halide-based perovskites and to address the above issues, a non-halide-based anion element should be partially substituted, which gives a covalent character to the B-X bond, as the chalcogenide bond formation, can be regarded as partially covalent. This partial substitution of chalcogenide could empirically be defined as a split anion exchange^{87,88} method, which generates a new family of semiconductors “**chalcohalides**”. Based on high-Z ns^2 electron configuration and during the interaction with electromagnetic radiation, the occurrence of spin-orbit coupling which enhances the polarization of the charge carriers in semiconductors with some basis of (ferroelectrics) Pb^{+2} cation for consideration, and with similar conditions, even upon the ability in forming +3 charge, despite this, heavy pnictogen elements (Sb^{3+} and Bi^{3+}) makes a suitable consideration for charge generation and transfer conditions⁸⁵. Moreover, they offer poor dichotomy, structural stability in harsh environments, and high charge carrier mobility, which pushes these materials as a promising alternative with non-toxic and earth-abundant characteristics⁸⁵, when compared to the Lead halide-based and hybrid-perovskites for photovoltaics⁸⁶.

Due to the distinctive electronic structure in chalcohalides, which arises the anti-bonding condition, upon hybridization of s-p orbitals, obtained by valence band maximum of the cation with the conduction band minimum of anion, which exhibits defect tolerant and high charge carrier mobility situation. The involvement of multiple anions i.e., mono-valent

and di-valent elements, allow for the tailoring of the chemical composition of chalcogenide-based compounds, which leads to the usage of these nanocrystals in multiple applications⁸⁵. Synthesis of inorganic nanocrystals through synthetic procedures limits their usage in device fabrication due to their poor post-synthesis processibility. A further discussion on the issues related to the synthesis of MQX (M= Sb or Bi, Q= S, Se and Te and X= Cl, Br and I), is given in the immediate next section of this chapter.

1.3. Research issue.

Chalcogenide NCs represent a new class of semiconductor materials, with an expectation to near reach the efficiency of perovskite NCs and other semiconductor materials family, as their chemistry at the nanoscale is still unexplored completely. However, most of the semiconductor NCs are being developed through traditional synthetic methods, which rely on slow crystal growth conditions at high temperatures (>400°C), which is a time and energy-consuming process⁸⁹. In addition, recently most of the semiconductor NCs are being grown directly on the conductive substrates through the dispersion techniques, which resulted in poor crystal morphologies, as this limits their access to device construction⁹⁰. Moreover, the post-synthesis processibility of NCs with the above procedures is comprehensively much more difficult to attain the suitable properties for the photovoltaic, optoelectric, photoelectrochemical, photocatalytic, and biomedicine applications.

Another major challenge, faced during the synthesis of NCs is the phase stability of nanocrystals, for which to acquire a phase pure NCs, a proper stoichiometric ratio needs to be attained, which could be reached only in solution process methods rather than the solid-state or vapor-state procedures. However, the structural stability of the NCs needed to be maintained the same, in ambient and in high-temperature conditions ($T < 380^\circ\text{C}$)^{61,62}.

To the end, the presence of Pb and Cd-based compounds in photovoltaic devices led to a serious concern about toxicity issues, identification of Lead-free semiconductor materials is still an active area of research interest^{59,60}.

1.4. Aim of the thesis.

This thesis work aims to address some of the above-outlined issues. Primarily, by considering Antimony Sb^{+3} , as a non-toxic, high absorption coefficient and efficient charge carrier mobility element. Besides, the selection of a suitable method for the synthesis of phase pure and stable NCs, will be addressing by opting colloidal growth method, through which we will try to understand the following, transformative mechanism from the precursor/reagents stage to the well-confined NCs which include, phase transformation and surface passivation of NCs. Lastly, by carrying out a suitable investigating procedure, by conducting some optical, morphological, and electrical characterization works to validate the obtained Antimony sulfobromide NCs, to identify its credibility for further embedment in devices.

1.5. Outline of this thesis.

This thesis contains six chapters, mainly focused on the colloidal antimony chalcogenide nanocrystals. The first chapter is an introduction to colloidal nanocrystals, followed by the emergence of semiconductor nanocrystals in the photovoltaics domain and pointing out the associated issues which need to be addressed.

The second chapter briefs, with the introduction of physics involved in nanocrystals. This chapter also covers the charge confinement effects and luminescence quantum yield and its principles.

Chapter 3 shows the chemistry behind the colloidal semiconductor nanocrystals, in this chapter the discussions involved are about the facile and efficient synthesis procedures and the chemistry involved during the synthesis process. And continued, with the selection of suitable surfactants for the growth and passivation of NCs. Ends with the surface ligand modification through ligand-replacement.

Chapter 4 is about the characterization methods which are used to validate the obtained nanocrystals. It is done by using respective microscopes and spectrometers.

Chapter 5 describes the research work on, synthesis, and post-processing of colloidal SbSBr nanocrystals. This chapter aims on brief understanding in attaining stoichiometric ratio and halide deficient defects and effects, to end it also covers the surface passivation of SbSBr NCs and ligand exchange conditions. Along with the characterization works of

colloidal nanocrystals, which includes structural, optical, and compositional-based properties of the colloidal nanocrystals are interpreted.

In the last chapter 6 Conclusion and future prospects, and to the end attached references which were used in framing this thesis.

2. Physics of colloidal semiconductor NCs.

2.1. General physics of colloidal semiconductor NCs.

Semiconductor materials exhibit diverse responses when their size is limited to the nanometer range and are named semiconductor nanocrystals (NCs). Colloidal semiconductor NCs, also are referred to as quantum dots (QDs), have sizes ranging from 2-10 nm and exhibit unique physico-chemical properties, due to their size dependency. Additionally, the surface-to-volume ratio of the nanocrystals increases, and the conc. of the surface atoms become more significant than in bulk semiconductor materials, which imposes greater columbic forces between the charge carriers, to this observation the band gap of QD is higher in comparison to the bulk material. The size of nanocrystals falls into the nanoscale range, upon which they experience the quantum effects due to the confinement of the crystal size to a particular spatial range, known as Bohr radius r_B , which causes the carrier structure to be modulated from band-like to discrete energy levels.

In the present chapter, we have focused on understanding some of the quantum confinement conditions involved in the execution and explanation of semiconductor nanocrystals (QDs), as well as their responses.

2.2. Quantum size effects.

To understand the charge carrier structure of confined particles in the nanometre range, it is suitable to understand and interpret with well-defined reference i.e., CdSe (macroscopic crystal), and then by following the top-down approximation one can receive the basic understanding of QD photo-physics.

In a macroscopic crystal, due to the linear combination of atomic orbitals (nearly infinite), provides a continuous distribution of energy levels (bands) whose energy difference is minimal (E_g). The least unoccupied and heavily occupied energy levels in a crystal, evolve into the conduction and valence bands, and these energy levels are distanced with a gap value of energy ' E_g '. At the equilibrium, the valence band is filled with electrons, upon irradiation with an equivalent or higher energy photon, the generation of effective charge carriers takes place, and the transmittance of electrons from the valence band maximum to

the conduction band minimum happens, the produced excitons move in the periodic potential of the crystal lattice and contribute to the charge generation and transfer.

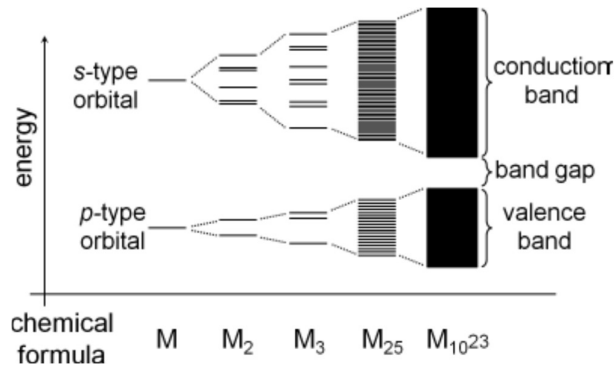


Fig. 2. 1. Schematic representation of the band structure of the bulk crystals, which depicts the continuous energy levels¹.

The concept of band gap and electronic structure, which were introduced for the macroscopic crystals can still be assumed/consider for the nanostructured (QDs) materials. In addition to the above, the concentration (conc.) of surface atoms is never ignored at nanoscale level, their dispersed energy levels are approximated as,

$$E_c = \frac{\hbar^2 k^2}{2m_c^*} + E_g \quad (E_c = \text{conduction band}).$$

In bulk semiconductor crystals, the energy levels are the continuous distribution of energy bands with a scale of k^2 (fig.1) The curvature of the energy bands is dependent on the 'effective mass' of the photo-generated excitons.

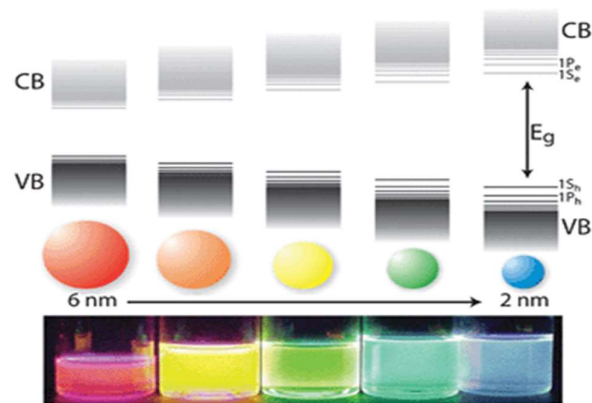


Fig. 2. 2. Schematic observation of the effect of quantum confinement on the electronic structure of semiconductor material².

The major observation of the QDs upon the spatial confinement is, the excitons are impacted by the fixed boundary conditions: the wave functions of the excitons must drop to zero at the edge of QD. Therefore, confinement causes changes in the density of electronic states and in the energy levels separation when the size of a QD approaches the de Broglie's wavelength of the associated charge carriers. These changes are exhibited by an increase in the bandgap E_g with decreasing size and the emergence of discrete energy levels near the band edges⁹¹.

Quantum confinement effects come into existence in a crystal, upon the reach to a particular spatial volume i.e., equivalent to the scale of natural electron and hole region, known as Bohr radius r_B . When the nanocrystal attains a radius greater than r_B , quantum confinement effects are weak due to the availability of the excess spatial volume for the possibilities to attain the exciton wavevectors/functions of that particular region. If the QD radius is less than any one of the exciton charge carriers and greater than other, it will undergo intermediate confinement effects and when the QD is confined to less than the Bohr radii, the crystal will undergo a strong confinement regime.

2.2.1. Particle in a sphere.

The quantum confinement effect is modelled theoretically by considering the QD inside a box, with a considerable potential energy of 'V'. For illustrating the relation between confinement and quantized energy levels, this method is considered as a suitable one. Let us, consider a particle placed inside a spatial volume object assume it as a box, with the following potential conditions given below

$$V = \begin{cases} 0 & \text{if } 0 < r < a. \\ \infty & \text{elsewhere,} \end{cases}$$

In the above, where 'a' is the radius of a potential well, in effect to the present condition the electron and hole will undergo the adjustment of the charge carrier wavevectors till the boundary walls of the box. Indeed, the potential energy of the confined charge carriers within the dot is lower than the surrounding medium. In quantum mechanics energy states of the particle is described by the Schrodinger wave equation, whose energy condition is given as,

$$E_{n,l} = \frac{-\hbar^2 k^2}{2m}, \text{ where, } k = \frac{\beta_{n,l}}{a}. \text{ (Equation 2-1.)}$$

In the above equation, where n and l are quantum numbers and k is wavevector of the edge energy level. Another reason for the consideration of potential well theory for QD is to

express the condition of charge tunneling (considered for the charge transfer) between, two adjacent QDs and its behavior with certain spatial volume. Moreover, the confinement condition generates the columbic forces such as attraction and repulsion, which furnishes the weak perturbation in the crystal significantly, these effects are also considered for the energy gap widening in the QDs. As the energy levels in QDs are modulated into discrete levels and they are designated with the help of quantum numbers n, l and m, which are further characterized into the orbitals.

Due to the confinement condition the quantized energy levels are varied according to the effective mass of the charge carriers which occur upon the introduction of weak perturbation through confinement procedure. To identify the position of the particle in the spherical potential well, however particle could be traced by using the Schrodinger wave equation with respect to time.

$$\psi(x, t) = \psi(x)e^{-\frac{iEt}{\hbar}} \text{ (Equation 2-2.)}$$

In the above equation, x and t are the position and recorded time of the particle, where E is energy of edge level. In addition, another approximation in the present model is that periodic arrangement of lattices in the QDs which generates the crystalline potential is the same as similar to the bulk crystal. The effective band gap of the spherical particle can be described by using the Brus equation,

$$E_{\text{QD}} = E_{\text{B}} + \frac{\hbar^2}{8r^2} \left(\frac{1}{m_e^*} + \frac{1}{m_h^*} \right) - \frac{1.8e^2}{4\pi\epsilon_0 r \epsilon_B} \text{ (Equation 2-3.)}$$

In the above equation, E_{B} is the band gap of bulk material, m_e^* , m_h^* are the effective masses of the excitons, and ϵ_0 and ϵ_B are the charge dielectric permittivity values. To the end, by using particle in a box model, one can understand the quantization of energy levels effected by upon confinement, which provokes the explanation of wave like behaviour of the particle by identifying the position of the particle at particular time⁹².

2.3. Practical evidence for the confinement.

2.3.1. Absorption spectrum.

As the various semiconductor materials possess different band gap E_g , and their respective localized electronic states, which are laid in the region from visible or near infrared. In order to attain a proper validation of the nanocrystals, optical spectroscopy is among the most suitable measures to understand its electronic properties. Moreover, the energy between the higher and the lower energy levels in a nanocrystal is of the order of eV, which can be clearly distinguished with the help of the optical absorption of photon energy by that particular type nanocrystal.

As the charge transition in semiconductors is subjected to certain conditions, the general condition which needs to be satisfied by a photon wave vector, k , for an effective conduction is $h\nu > E_g$, is required. As the wave vector of the photon is small when compared to the wave vector of electron before (k_e) and post excitation k_e' . The semiconductors in which the photon energy is conserved, due to the transition of charge from high energy level to low energy level and vice versa, these categorized under edge-on-edge energy state (direct band gap) semiconductors, and possess large absorption coefficients. And when it comes to the semiconductor materials with low energy electronic transitions, are considered as diagonal edge-on-edge level (indirect band gap). In continuation of the charge transfer, if we consider the momentum condition the existence of the phonon participation is needed to undergo the lattice vibrations in a crystal.

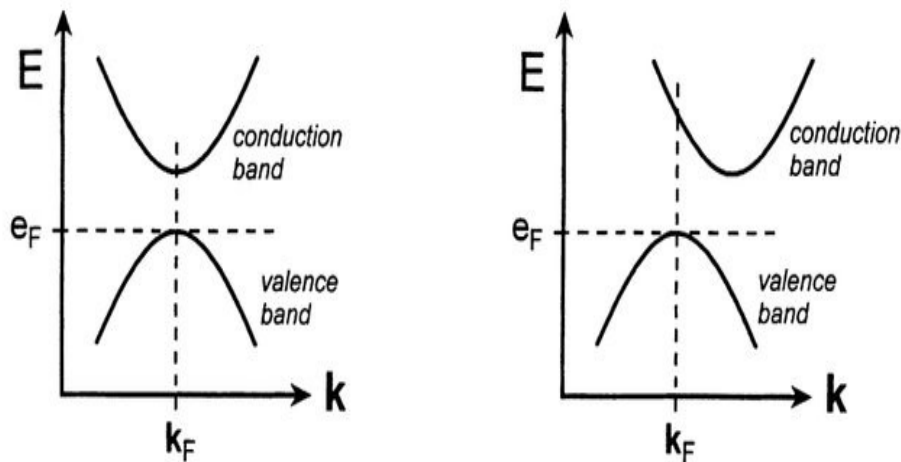


Fig. 2.3. Schematic view of the edge-on-edge and diagonal edge-on-edge transition of semiconductor material³.

As the properties are based on the size of the nanocrystals, in smaller QDs the energy required for the absorption is at higher energy. It is evident that, as the size of the nanocrystal reduces the energy gap between the two levels is distanced largely, which can be proved with the help of absorption spectroscopy. In addition, the oscillator strength which is proportional to the energy level increases with respect to the crystal size, due to the compact overlapping of the wave vectors of the quantized energy levels.

Now, when it comes to the lowest absorption energy peak and the luminescence peak are bounded to the mean of NC dimensions, if it comes to the inhomogeneous broadening of the peaks are related to the adverse effects of the size distribution. NCs with monodispersed condition omits sharp peak, through which we can confirm the absorption spectroscopy as a powerful tool for validation of the nanocrystals.

In order of interpreting the data obtained from the absorption spectrum of QDs, a detailed consideration of the transitions between the energy levels based on quantum size is needed. The obtained spectrum is calculated with the help of parabolic approximations, but in real time considerations it is not applicable in the QDs semiconductor materials. At this point of spherical QD, with the absence of band mixing effects, the low energy level initiates an electron quantization conditions, that can be explained by using principle (n) and azimuthal (L) quantum principle's¹.

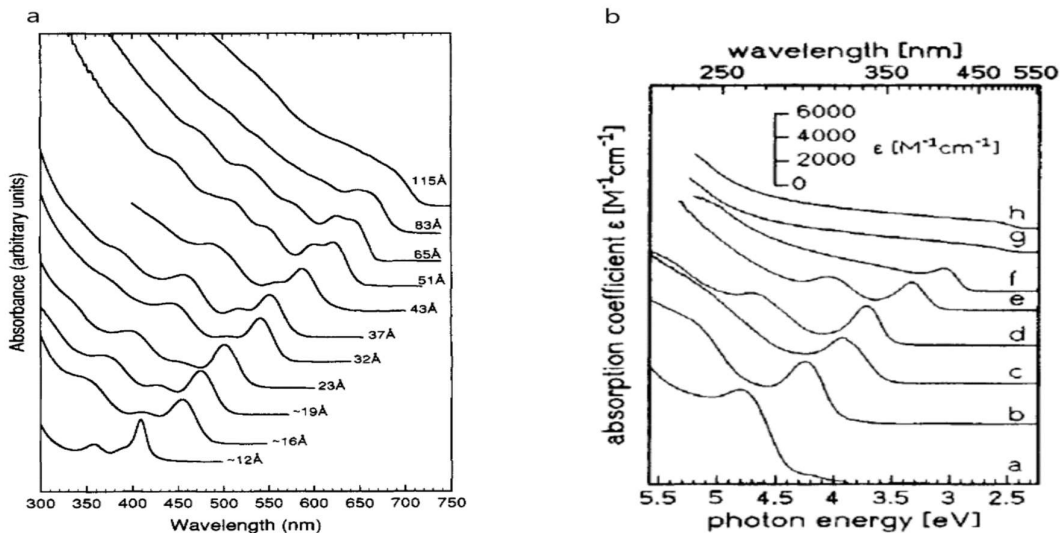


Fig. 2. 4. a. Schematic observation of the CdSe NCs at room temperature absorption spectrum. b. Electronic spectrum of CdS at varied size³.

The angular momentum is denoted by a letter (S for $L = 0$, P for $L = 1$, and so on) and is followed by the value of n in standard quantized state notation. The electron quantum state levels are thus expressed as " nL "; the three lowest states, in order of increasing energy, are: 1S, 1P, and 1D. However, due to the more complex, multi-sub-band situation of the valence band and the mixing effects, hole quantized states are better described by considering the total angular momentum \bar{F} equal to the sum of the orbital momentum of the hole envelope function, L , and the Bloch function angular momentum \bar{j} . Hole quantum state levels can be written down as nL_F . Ekimov et al had produced size dependent hole states of CdSe NCs, the three possible lowest hole energies are $1S_{3/2}$, $1P_{3/2}$ and $2S_{3/2}$.

A typical electron-hole transition from the above can be observed as $1S_{(e)} - 1S_{3/2(h)}$, which is considered as the edge-on-edge transition. Similarly, transitions of $1S_{(e)}$ and $2S_{(e)}$ energy levels are also possible from $nS_{2/3(h)}$ and $nS_{2/3(h)}$, by following the quantum energy levels. And the same is followed with the other higher energy levels. A schematic observation of the CdSe QD optical transition and quantum size energy levels is shown in the **fig. 2-5**.

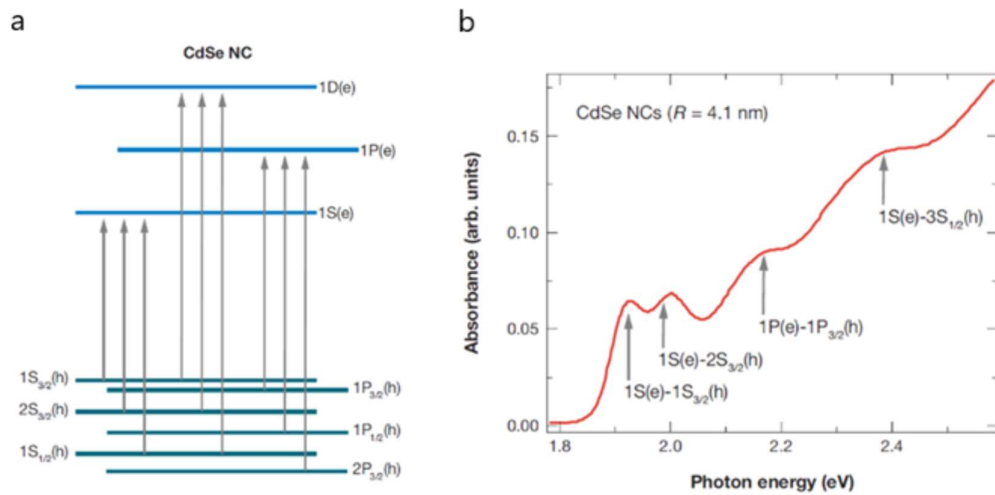


Fig. 2. 5. a. Schematic observation of the allowed inter-band transitions in CdSe. b. CdSe absorption spectrum with the well resolved transitions³.

2.3.2. Photoluminescence and Stokes shift.

Photoluminescence is a short-lived spontaneous radiative recombination process that happens when an electron-hole pair recombines and emits a photon. However, the presence of lattice defects in nanocrystals (mostly at their surfaces) causes charge carrier recombination in competitive non-radiative pathways, resulting low quantum efficiencies. Many investigations corroborated the previous assertion, demonstrating that surface modification, such as the formation of a wide-gap semiconductor covering the NC surface or passivation with organic ligands, enhanced excitonic photoluminescence on semiconductor nanocrystals.

An interesting aspect of semiconductor NCs is the redshift of emission peaks with respect to absorption spectra (also known as Stokes shift) and its size dependence; this shift diminishes with increasing dot radius and disappears beyond a certain radius. The Stokes shift is caused by the complicated electronic structure of excitons in semiconductor nanocrystals, as well as the related transition probabilities between levels¹.

Radiative recombination causes light to be emitted, hence the material must be trap free. To measure radiative recombination and hence establish a figure of merit for emission efficiency, the rates of radiative and non-radiative recombination must be compared. The decay rate y_{rad} describes the rate at which energized electrons radiatively recombine and similarly, non-radiative recombination is referred to as y_{nr} . As a result, the ratio between y_{rad} and the total of all recombination rates, as stated in equation below, characterizes a material's quantum efficiency (η) or photoluminescence quantum yield (PLQY)⁹².

$$\eta = \frac{y_{rad}}{y_{rad} + y_{nr}}$$

As the Photoluminescence of a material is totally dependent on the material quality, and the procedures followed for the preparation and processing it.

3. Chemistry of colloidal semiconductor nanocrystals.

3.1. Introduction.

Nanocrystals are among the fundamental building blocks of Nanoscience and Nanotechnology, their synthesis and growth kinetics are the prime aspects of interest to understand the major portion of Nanochemistry. In majority conditions, development of nanocrystals is achieved through bottom-up approach, which is followed in order to attain the miniaturization of functional devices which descends to nano size. In order to understand the size dependent effects of the nanocrystals, it is evident to know its growth kinetics and the surface chemistry, which explicitly details about the composition, size or shape-controlled growth of NCs and their surface-ligand interaction.

Over the last few decades, synthesis of nanocrystals involves the polar solvents such as, aqueous medium through which, the achieved NCs are of low crystallinity and minimal uniformity in particle morphologies. In order to overcome the above effects, usage of non-aqueous solvents for the synthesis of in-organic nanocrystals, led to high crystallinity, with well-defined crystal morphologies. As the above is achieved by using the organic solvents, whose components involve during the crystal growth and orientation⁹³.

In the present chapter, we discuss about the general aspects of the colloidal in-organic semiconductor nanocrystal growth in organic solvent, along with the surface passivating surfactants. Moreover, in order to attain defect free nanocrystals, the role and condition between the surfactants, precursors and solvent as well as their interface need to be understood. In addition, the growth kinetic process and the thermodynamic diffusion of the monomers is also focused, in order of attaining the size/shape controlled and phase pure nanocrystals.

3.2. Synthesis of colloidal semiconductor nanocrystals.

In general, synthesis of colloidal nanocrystals is a major inter-play between the physics and chemistry. In order to make the synthesized nanocrystals capable enough to be embedded in the functional devices, they should possess certain credibility to meet the end usage conditions with the developed properties of NCs.

Over the last two decades, nanocrystals are synthesized through various methods which are mainly categorized under 1. Top-down and 2. Bottom-up approach. In the top-down

method, the nanocrystals are attained through the reduction of micro (bulk) particles to the nanoscale level, by using various methods such as milling, etching etc. From the above procedure, the individual cannot attain the required composition and the size/shape of the nanocrystals easily or alter according to the desired composition needed. To control the above, bottom-up approach is followed on which the desired composition and structure is obtained from their constituent atoms, which ends up producing colloidal nanocrystals.

Bottom-up approach is attained by two major techniques i.e., 1. Heat-up method and 2. Hot-injection method. In heat-up method, the general procedure which is followed is: addition of the required reagents, surfactants and solvent together and heated up for the crystallization procedure. If it comes to the Hot-injection synthesis technique, the anion precursors are generally added at post complete dissolution of the metal reagent and stabilizing agents, in which the rapid nucleation and the controlled growth of the nanocrystals is attained. In the hot-injection method the obtained crystals are of low polydispersity and phase pure. To the end heat-up method is majorly accepted at the industrial level, to meet the continuous production, high quality NCs and simple procedures to follow.

In continuation to the above, in the following sections of this chapter are focused on the Hot-injection method, growth mechanism in respect to the principals and empirical conditions.

6.2.1. Hot-injection synthesis of semiconductor nanocrystals.

Hot-injection synthesis technique is majorly used in respect to the attainment of the highly monodisperse (nearly >95%) nanocrystals and tailored procedures to receive defect free nanocrystals⁹⁴.

In the present technique as said above, reagents, stabilizing agents and solvent are added in a three neck round bottom flask and heated-up the added flask to the desired temperature (i.e., reaction temperature (RT) 150°C-230°C) with the help of a heating mantle. The reaction procedures were done in a controlled and in an ambient condition such as, considerable vacuum and continuous nitrogen purging is maintained in a well-defined Schlenk line setup, which is done to avoid the oxidation and hydrolysis in the reaction flask, moreover constant observation of the temperature in the reaction flask is followed.

As the core surfactant precursors are added into the reaction flask, supersaturation of monomers occur which is leading to instant or rapid nucleation also known as burst

nucleation, followed by phase growth. For the better understanding of the nucleation and growth mechanism of nanocrystals, the LaMer model and Ostwald condition is detailed below.

6.2.1.1. LaMer and Ostwald Theories.

The prime condition to understand the nucleation and growth mechanism, which was explained by the V.K LaMer, his theory involved the synthesis of monodispersed sulphur-based colloids, from thiosulphate complex. During, the above experiment his observations are, on the nucleation and growth of sulphur particles, through which he had divided the nucleation process into three stages. During the stage 1, the critical concentration of the monomer molecules is mandate to start the nucleation of nanocrystals, once the critical point is reached, the hetero-nucleation stage starts (stage 2.), at this point the nucleation rate is defined as “burst nucleation”, and after stage 2, his observation was regarding to further nucleation which is very low, as the concentration of the monomers in the solution is reduced due to the initial consumption of the monomers for the growth of low surface curvature nuclei. In continuation to the above, additional nucleation process takes place with the help of diffusivity of the monomers in the solution i.e., stage 3. The above explanation could be observed clearly with the help of below image.

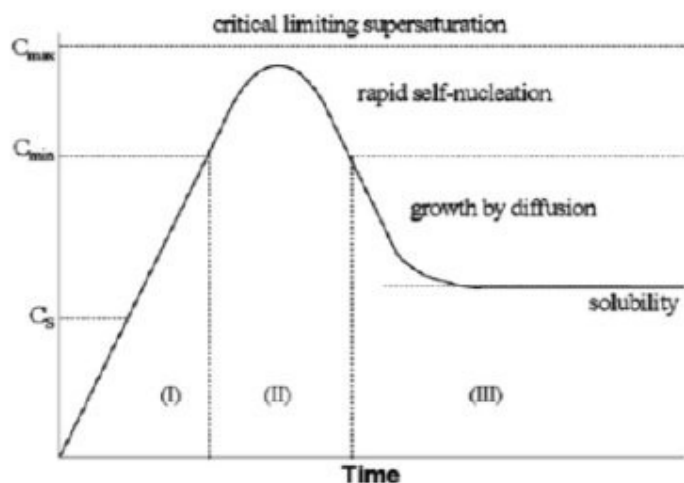


Fig. 3. 1. Schematic representation of the LaMer theory of nucleation and growth mechanism w.r.t to the concentration of the monomers vs time⁴.

Limiting the growth of the nanoparticles is significant enough to obtain the monodisperse and almost near similar size distribution⁴. Ostwald ripening is one among the general process, which explains about the growth mechanism of NCs. Colloidal particles are inspired

to descend their surface-to volume ratio, to attain a particular surface-energy. This condition was well explained by Lifshitz-Slyozov-Wagner (LSW) theory, about the relation between the particle growth with respect to their surface energy, and solubility of particles with respect to their size. A nanoparticle in a solution, whose radius is larger than the critical radius will grow on the redissolution of the smaller radius particles⁹⁵, is generally known as Ostwald ripening. The general equation for the critical radius of a particle in a solution is given as,

$$r_{crt} = \frac{2\gamma v_m}{RT \ln S}$$

From the above equation, r_{crt} is the critical radius to be attained by the particles, γ is the specific surface energy of the crystal, R is the universal gas constant, T is temperature, V_m is molar volume and S is the supersaturation condition of precursor molecules in the solution. Nucleation and growth of nanoparticles in a solution, could also be explored with the help of classical theories.

6.3. Classical Theories of nucleation and growth of nanocrystals in solution.

Growth of nanocrystal is explained with the help of Ostwald theory, i.e., it grows upon the sacrifice of the high curvature particles. Moreover, the size evolution of NCs depends on the multiple parameters, such as interfacial energy of the NCs in the solution, chemical potential of the monomers and their respective atomic elements embedment in the crystal, the above effect nucleation and growth of nanocrystals to certain extent and in addition the diffusion of monomer species to the surface of the nanocrystals and the monomer incorporation into crystal growth, will impact⁹⁵ on the growth limits of nanocrystals⁹⁵.

The growth of nanocrystals is considered with the help of capillary action, which explains about the equilibrium condition of finite phases, in the path of nanocrystal generation with the monomer molecules. Furthermore, the interfacial energy of the individual facets which directs the growth and shape of a nanocrystal, will also be considered in the present topic. In the present chapter, whenever we refer to nanocrystal (NCs) it is considered, its outer structure as spherical.

To the end nucleation and growth mechanism of nanocrystals in solution is considered in two forms 1. Homogeneous nucleation and 2. Heterogeneous nucleation, about which we will be observing below.

6.3.1. Homogeneous and Heterogeneous nucleation of Nanocrystals.

In the present topic we examine in detail about the nucleation event. In general, the nucleation events are distinguished in two types i.e., 1. Homogeneous and 2. Heterogeneous nucleation. Firstly, we consider the heterogeneous nucleation, which is a path directed nucleation. It occurs upon the addition of the seeds of the core element or the substrate. If we consider the homogeneous nucleation, which takes place without any pre-existing path for nucleation. The growth of the nanocrystals in the homogeneous condition takes place, when a favourable kinetic and thermodynamic conditions are maintained in the solution, which include the temperature, fraction of monomers available for further reaction and the interfacial energy of the nanocrystals (critical radius r_{crt})⁹³.

By not spending more words on the details of many theories, in the present work we consider few fundamental theories which are in the major cause for the nucleation of nanocrystals. Moreover, the present thesis work is based on the homogeneous nucleation conditions, as we avoid the addition of seeds of the core substance into the solution. We can assume that in order to generate the nuclei, the substance for the formation, is in need to overcome the energy barrier. This barrier is a condition for the newly forming nuclei, which has to overcome for the generation of new interface between the solution and the forming nuclei. Further, we can infer the availability of the barrier, by just simply mixing the monomers with the suitable reagents, which is not enough for the formation of nuclei. For which an appropriate conditions need to be maintained, among which some are considered empirically through the multiple attempts. From the above formal discussions, important parameters are, temperature, chemical potential of crystal elements in the solution μ_{sol} and the chemical potential of the elements in the crystal $\mu_{crystal}$. To understand the potential difference between the two and to analyse the required monomer concentration for the nucleation, to overcome the barrier, let us consider the following equation^{4,95},

$$\Delta\mu = \mu_{sol} - \mu_{crystal}.$$

The above condition is valid for the supersaturation condition, in which the concentration of the monomers is above the equilibrium value, which is necessary for the aggregation through the thermodynamic conditions. From the above, once the supersaturation limit in the solution is reached, and the enough thermodynamic equilibrium is attained, the system will prevail for the nucleation process. If the system had surpassed below the

supersaturation limits, the other parameters come into existence such as, temperature, time and interfacial energy for the control of crystal growth, later on which could also be modified with the help of surfactants and the reactivity of the monomers in the solution.

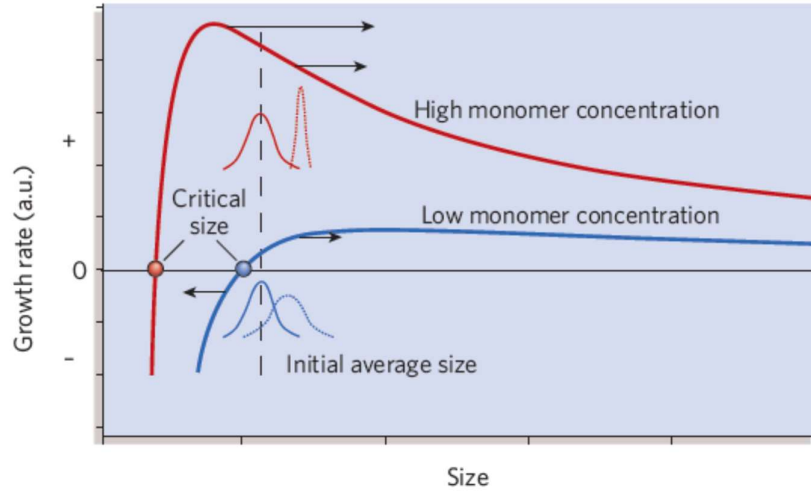


Fig. 3. 2. Schematic representation of the nanocrystal size dependence on the monomer concentration and its growth rate⁴.

The energy required to overcome the barrier and for the formation of nuclei is considered, Gibbs free energy ΔG , it is sum of two terms. The chemical potential attained by the elements present in the solution for the nucleation process is denoted with ΔG_v .

$$\Delta G_v = n^* (-\Delta\mu)$$

The other contribution for the nucleation condition is surface energy ΔG_s , which is defined as free energy required for the development of interface between the solution and the condensed phase. In this condition, interfacial energy is a parametric consideration of interfacial area of the spherical nanocrystal.

$$\Delta G_s = 4\pi r^2 \gamma_{NI}$$

In the above, r is the radius of the NC, γ_{NI} is interfacial energy considered for unit area. By combining the two terms, we obtain the required nucleation energy ΔG .

$$\Delta G = -\frac{4\pi r^3}{3v_{cryst}} \Delta\mu + 4\pi r^2 \gamma_{NI}$$

The barrier energy (ΔG) is considered as the activation energy. From the above equation it is observed that the nucleus with the radius above the critical radius r_{crit} , will grow larger and if it comes to the one which couldn't meet the critical radius will redissolve in the

solution. In the next section of this chapter, will be discussing about the control of size and shape of the NCs.

6.4. Size and Shape Control.

Now we consider the growth of nanocrystals in detail. During the initial point of growth stage, the monomer concentration in the solution is at supersaturation stage. Therefore, the first term in the activation energy i.e., volume term ΔG_v , in the above condition of supersaturation is higher than the second term ΔG_s (surface energy), and with this condition the total energy ΔG will be negative and the crystal will be growing^{94,96}.

As the reaction mechanism in the reaction chamber goes on, the monomer concentration keeps on decreasing with respect to the crystal growth, and further generation of new nuclei will be forbidden or minimal. From this point, the nucleation which takes place in the reaction chamber will be with diffused monomer (diffusion limited regime) conditions and the reaction which takes place on the nanocrystal surface is reaction limited regime under kinetic aspect.

If we consider the diffusion limited growth regime, the kinetic aspect of limiting condition comes into existence i.e., the transfer of monomers from the bulk solution region to the surface of the nanocrystals. From the above point, the radius of the nanocrystals under the kinetic and thermodynamic aspects on growth of nuclei is given as,

$$\frac{dr}{dt} = \frac{K}{r} \left(\frac{1}{r^*} - \frac{1}{r} \right)$$

where K is kinetic and thermodynamic aspects and r^* is the critical radius of the nanocrystal. We can also consider the critical radius of the nanocrystal over a period of time by considering the radius at two points with respect to the time. To the above Δr is the difference of the two observed radius and its mean is given as $\bar{r} = \sqrt{r_1 r_2}$, and the critical radius with respect to the present condition i.e., rate of change of radius Δr is given as⁹⁷,

$$\frac{d\Delta r}{dt} = \frac{K\Delta r}{\bar{r}^2} \left(\frac{2}{\bar{r}} - \frac{1}{r^*} \right)$$

As we leave the reaction to be carried on for a prolonged period of time, the crystals which are obtained would be of with large size (polymorph structures). To control the above, certain conditions are need to be followed, firstly we look about the crystal growing aspects and we discuss about the crystal growth control by adjusting the same parameters with the help of external entities and sources. Now, here we observe about the effects from the point of

surface energy, as we are working with the nanosized structures, the curves developed at the edges and corners should also be considered. As they also possess an active region of crystal growth area facets. The overall surface energy including the edges and corners should be considered. By which, one can estimate the reactivity condition of the crystal facets.

The other aspect for the size and shape control is monomer (precursor) concentration in the reaction chamber. The term concentration of precursors is in existence with the base of kinetic parameters, as the diffusion of monomers is carried out without any halt, moreover high reactive facets of the crystals keep on reacting with the monomer molecules and grows further and the facets with low reactivity condition (high surface energy) will try to dissolve back. To avoid the above observation, addition of the surface stabilizers is mandate to control the growth reaction in the chamber, due to which the grown crystals get passivated with the stabilizing molecules and allows the new nuclei to grow further till the expected size and shape is attained.

In order to obtain the appreciable size and shape, there are multiple procedures to be followed, among many we discuss here few, which are required for our thesis work, Oriented attachment also known as selective attachment procedure and the other one is Thermodynamic approach. In the selective attachment condition, which leads to the anisotropic growth of nanocrystals, takes place due to the fusion of the same energy possessing facets and grow in the shape of rods, wires, and rings etc. When it comes to the thermodynamic term, by maintain the required thermal input and the monomer flow flux which creates the non-equilibrium condition in the reaction chamber and the crystal growth is in anisotropic form. In order to control the shape and size of the nanocrystals with the aspect of thermodynamic approach, we can alter the monomer concentration and the thermal input⁹⁷.

There are multiple stabilizing agents used for rapid reaction to take place, and to halt the growth of nanocrystals through passivation, about which we will be knowing in the next sections of this chapter.

6.5. Ligand replacement.

The surface of the pure NCs is an active area, which is coordinated with the elements well known as ligands. To not to expose the core surface to the environment, these ligands are utilized to maintain the neutrality of the core NCs properties. So, it is mandate to understand the relation and their bonding conditions i.e., between core structure surface and the ligands. By which individual can predict the stability and electronic properties of the core-ligand structure, when they are dispersed in apolar solvent. The surface of the NCs and the ligand should be holding a neutral condition, in order to avoid the oxidation and altering its core physical structure (phase)⁹⁸.

In order to balance the charge by considering the charge balance model, the metal rich core possess the positive charge to balance it, a negative charge anionic substance (ligand) is added over the surface. Moreover, the bonding between the core and the ligand is rationalized by using classification of covalent bonds (CBC). In addition, the ligands make a covalent bonding with the core structure by 2-centre-2-electron dative bond condition.

Generally, ligand replacement can be done in two ways i.e., liquid state ligand exchange and the solid-state ligand exchange. In solid-state ligand exchange procedure, the surface ligands are replaced by dipping the deposited substrate in the solution upon addition of replacing ligands. If it comes to the liquid state ligand exchange, after cleaning crude product and redispersing it in apolar solvent (toluene). A suitable amount of substituting ligand is added in the same apolar solvent of redispersed NCs, and it is vortexed for a period of time to carry out the complete or partial substitution of pristine ligands⁹⁷.

Another type of ligands on the surface of NCs, whose aim is to control the growth of nanocrystals, well known as surfactants. As these surfactants are used to cover the surface defects in order to attain the crystal structure and elite electronic properties. Due to their disability to cover the entire surface of the NCs, these long chain molecules alter the structure of the NCs. In our present thesis work, we will be observing and understanding the core-ligand interaction and its effects in attaining suitable properties, this will be covered in chapter 5.

4. Characterization methods.

4.1. Morphological characterization - TEM and SEM.

The high magnification of TEM, which ranges from 50 to 10^6 , and its capacity to produce both pictures (information in cartesian system) and diffracted pattern (information in reciprocal system) for the same region by varying the strength of the intermediate lens are its two major advantages⁵. Through the use of a condenser lens system, electrons are projected onto a thin specimen (less than 200 nm) in transmission electron microscopy (TEM), where they either penetrate the sample thickness undeflected or deflected after being accelerated with 100 KeV or more (up to 1 MeV) (fig.4-1.).

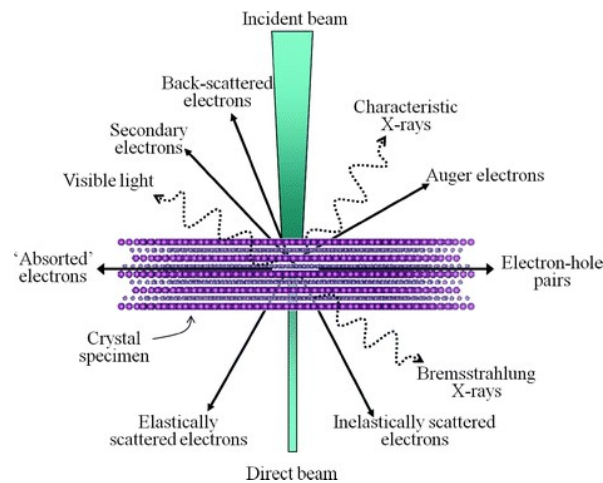


Fig. 4. 1. Schematic representation of the signals generated during the interaction of highly energized electron beam when subjected onto the sample⁵.

The narrow functional electron wavelengths, which is given by de Broglie's equation: $\lambda = \frac{h}{p} = \frac{h}{mv}$, where p , m , and v stand for the momentum, mass, and velocity of the electron, respectively. Higher-energy electrons with a wavelength of 0.005 nm that are excited and projected into vacuum from a heated filament and accelerated by a potential difference of 50 kV can penetrate solids at distances of several microns.

The type of information gathered depends on the scattering processes that electrons go through as they move through the material. Diffraction patterns result from elastic scattering, which does not lose energy. Primary electrons interact inelastically with free electrons at heterogeneous sites such as grain boundaries, secondary-phase particles, defects, density

fluctuations, etc., resulting in complicated absorption and scattering processes that change the transmitted electrons intensity spatially.

The image can be acquired by collecting only the centrally transmitted beam or by capturing the diffracted beams, to obtain electron diffraction maps. The reproduction of the image on the phosphor screen is due to contrast phenomena. The contrast in TEM images is due to several factors: the diffraction contrast is due to the perturbations generated because of the defects (point, linear or planar) and to the lattice deformations. In general, it has to do with the usage of a diaphragm, which only permits the passage of electrons that have been deflected at a specific angle. The phase modulation of the electronic pulse after it has passed through the sample is thus dependent on the atomic distribution of the substance (phase contrast). The high-resolution TEM depends on this contrast in order to achieve atomic resolution in the images. The final one is atomic number contrast or mass thickness. The number of electrons that reach the detector varies on the sample's composition as well as its thickness because different atomic numbers exhibit varying powers of scattering. Depending on the type of electrons analysed, a TEM tool allows to work in different modes for image acquisition, to obtain information of different type.

In image mode, the lenses after specimen are structured to inspect the material through the transmitted signal at objective lens's image plane. Eventually, the scattered electron waves recombine to create an image of the sample microstructure that contains distinguishable details (or atomic structure). The main visual modes are three; the often-used mode in TEM is Bright Field imaging one (BF, *fig.4-2.*), in which the contrast is generated directly upon the absorption of electrons in the sample, therefore thicker regions or regions with a high charge dense elements will appear dark, while those with no sample along the trajectory of the incident beam will appear bright. In this case, therefore, the image can be considered a simple 2D projection of the sample along the optical axis. A BF image is formed, only when the direct beam is projected through the objective aperture, which is inserted in the back focal plane or the objective lens. The images in Dark Field (*fig.4-2.*) are obtained instead by selecting the diffracted electrons through an aperture decentralized with respect to the central beam^{5,99,100}.

From the images acquired with a TEM it is possible to study the morphology of the samples, and therefore the shape and size of nanocrystalline materials, but also the electron diffraction fringes, obtaining information on the degree of crystallinity, and on any preferential orientations of the crystalline planes and crystallographic phases of the sample. For

crystalline samples, diffraction contrast can be used, where the electron beam undergoes diffraction by the crystal lattice according to Bragg's law, thus obtaining structural information. A diffraction pattern of a crystalline (or polycrystalline) sample can be generated by changing the order of the excitation of intermediate lenses, so that in spite of focusing on the first image plane of the objective lens, it is made to be focused on the back focal plane of the objective which retains the diffraction pattern.

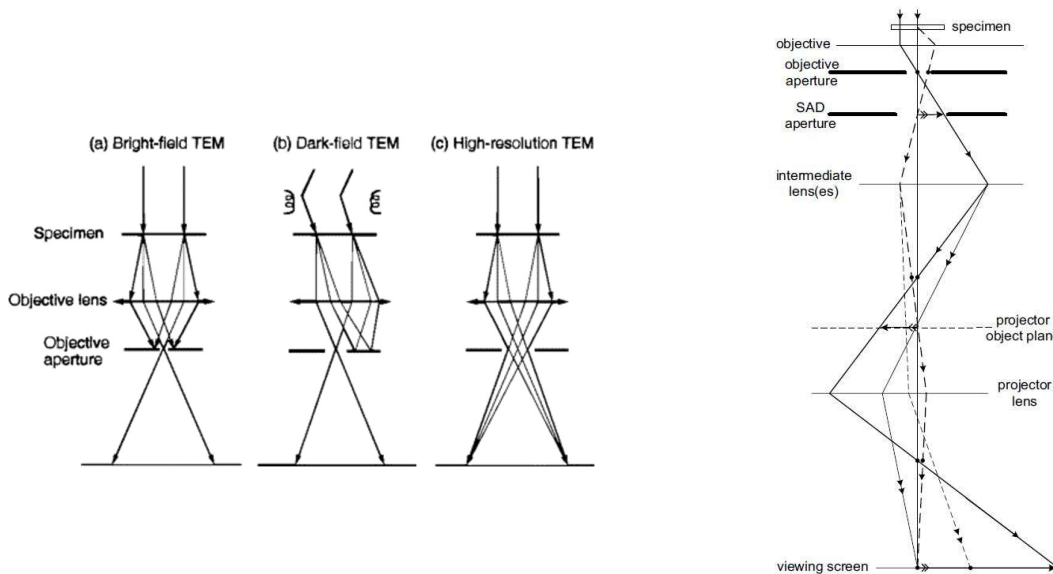


Fig. 4. 2. Optic ray diagram for obtaining a) bright field, b) dark field c) High resolution imaging in TEM, and d) sample imaging in TEM.

Selective area/electron diffraction (SAD or SAED) is a crystallographic technique which can be utilized for working in diffraction mode while performing TEM analysis. Using the SAD aperture, it is much possible to choose a sub-micron area of the specimen to get diffracted patterns form, *fig. 4-2* shows a simplified scheme of lenses to obtain the selective area of diffracted pattern. In this configuration, the focus of the intermediate lens coincides with the underlying focus of the objective lens. A second "intermediate aperture" is placed in the display plane of the objective lens, with the function of limiting the diffraction image to a limited region (selected) of the sample.

Energy Dispersed X-ray Spectroscopy (EDX or EDS) can be very useful in determining the precise content of a particular element in a specimen. All electron microscopes can perform EDX, which produces X-rays as an electron beam passes through a sample. When an electron is ejected from an inner shell, its ionization energy is comparable to that of the incident beam's electron, and the energy of the X-ray photon is the potential energy resulting

from the difference between the two ordered orbitals undergo the transition, which is unique to each element. The X-ray emission at different wavelengths might on then be measured through a photon-energy sensitive detector. These X-rays are observative for the element from which they originate, and they hold the information on availability and conc. of the different elements in the specimen^{5,100}.

An EDX graph is basically defined with an X-ray counts as a function of its energy in keV and the observation of a peak in the spectrum, its energy, recognizes the element; the area under the peak is with a definite relation to the number of atoms of the element in the irradiated area.

In the present thesis work, the samples were prepared by dispersing dilute solutions of NCs (maintained in a N₂-protected glovebox) onto carbon-coated grids and proceeding with the evaporation of solvent at room temperature. Low-resolution TEM images were acquired with JEOL microscope, JEM – 1400Plus, operating at 120 kV, respectively.

4.1.2. Scanning electron Microscopy.

The morphological results of a sample surface can be observed by utilizing scanning electron microscopy (SEM), an electro investigative technique. It also offers extensive information on the chemical composition close to the surface. The SEM can function at magnifications that can be readily changed from 10 to over 300,000. The resolution of the device is close to a few nano-meters. In a conventional SEM, an electron source is concentrated into a beam (primary electron ray) with a very small spot size of about 5 nm and energy spans from a few hundred eV to 50 KeV, which is then directed over the specimen's surface by guided deflection coils. There are a number of interactions that take place as the electrons hit and enter the surface, and they all lead to the emission of electrons.

Various SEM techniques are categorized based on the instantaneous detection and display of the specimen sample, and basically the images majorly obtained are by three types: secondary electron images, through backscattered electron and elemental X-ray positioning. Initially, when a high-energy electron interacts with an element, it faces either inelastic scattering with atomic electrons or elastic scattering with the atomic nucleus. If we consider inelastic collision with a same charge exciton, the primary electron transfers part of its energy to the other electron, which could be emitted by a sample. If the emitted electron possesses an energy value of lower than 50 eV, it is referred to as a secondary electron

(SE). Basically, backscattered electrons (BSE) are the highly energized ones, which even upon elastically scattered and significantly possess the same energy as the incident electrons. The probability of backscattering condition raises with respect to the sample composition.

The surface topography of the sample determines the SE's intensity; the amount of SE as seen depends on the material's orientation, inclination, and surface geometry in relation to the incident beam. These factors make secondary electrons useful for revealing surface topography and the presence and location of magnetic or electric fields. Contrary to BSE, the SE do not provide compositional information (since they lack the element's typical energies), but rather information on the sample's shape. Even though backscattering images cannot be utilized to identify elements, useful contrast can form between specimen sections with greatly different Z atomic numbers. An additional observation of electron interaction in the SEM analysis is, that the primary electron collides with and ejects an electron from the innermost atomic orbitals from the elements of sample⁵. The excitons of an atom will undergo a non-radiative recombination to its ground state by emitting either a characteristic X-ray photon (X-ray fluorescence) or an Auger electron (Auger effect), both of which have been used for chemical characterization. By exploiting the electron-matter interaction and collecting the X-ray emission signals, it is possible to couple the microanalysis (EDX) to the observations in imaging microscopy, which allows to do qualitative chemical analysis. The X-ray fluorescence and Auger emission processes are competitive, and the respective probability depends on the atomic number of the species occurring in the sample. The instrument therefore integrates detectors of secondary electrons, backscattered electrons, and X-rays, which allow to obtain the image of the sample together with the microanalysis. For non-metals SEM analysis, the usage of lower energy $\approx 1.5 - 5\text{keV}$ is preferred to avoid the damage of the sample,

4.2. Structural Characterization: X-Ray Diffraction (XRD).

X-ray Diffraction (XRD) method is a prominent experimental technique which provides information about the crystallographic structure status of the sample, through which we can identify the lattice strain, phase obtained, lattice positions in a crystallographic space and crystallite grain size.

While performing the XRD analysis, a sample would be placed in the centre of an instrument and illuminated with a collimated beam of X-rays, with wavelengths from 0.1 to 100 Å (1 Å

= 10–10 m). The X-ray source and the detector object travel in an optimized path with a coordination. The crystal in a lattice is a fact of a periodic arrangement of elements/molecules in a three-dimensional array of space, and each atom is made up of a nucleus surrounded by a cloud of electrons, whereas X-rays are composed of electromagnetic radiation substance. Crystal atoms upon scattering generates X-rays, specifically, through electron interactions, which is referred to as elastic scattering. The repetition of atomic arrangements in a crystal forms, different planes separated by principally defined distance. When an X-ray beam was impended over the atomic planes, the X-rays are coherently reflected by the regularly spaced atoms. These waves wipe out each other which form their wave path in the directions of destructive interference, but the left over would undergo constructive interference in few selective directions, in order of obtaining the constructive interference image as indicated by Bragg's law.

$$n\lambda = 2d\sin\theta \text{ (equation 4-1.)}$$

where, d is the spacing between lattice planes, θ is the angle of incidence, n is an integer, and λ is the wavelength of x-ray. The specific travel paths appear as spots on the screen made up with diffraction conditions called reflections. Generally, X-ray diffraction patterns result were from electromagnetic waves collided with a regular array of atoms. X-rays are used to produce the diffraction pattern in order to attain their particular wavelength, λ , and which is often in the same order of magnitude as the d -spacing, between lattice planes.

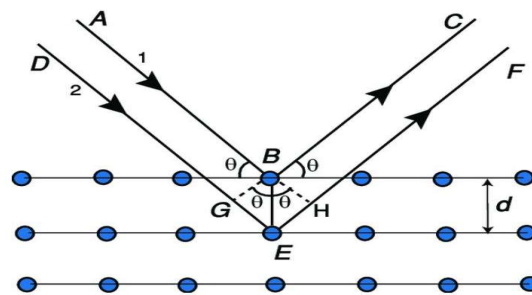


Fig. 4. 3. Bragg diffraction from a crystal with inter atomic spacing ' d '⁶.

In detail, X-rays striking the first plane are reflected at an angle of incidence- θ , and the same must be reinforced by in-phase reflections (integral values) of the other atomic planes for diffraction to be measurable. A ray following the path DEF, in the example of *fig.4-3*, will have travelled some whole number of wavelengths, $n\lambda$, ($GE + EH = n\lambda$) further than a ray travelling along the first atomic plane ABC. The angle observed in-between the normal to

the refractive wave front and the atomic positions will be equal to the angle between the normal to that of incidence wave front and the atomic planes⁶. Diffraction from a subsequent equally spaced lattice planes resulted in a maximum diffraction, which hold the required intensity to be acquired. The d-spacing is defined as the distance between atomic planes that cause diffraction peak; therefore, each peak in a diffractogram appeared from the corresponding d-spacing, which can be analyzed easily using the formula (equation. 4-1)⁶.

In the present thesis work, XRD instrument was used to obtain the nanocrystal structure. Powder XRD patterns were received, using Panalytical Empyrean diffractometer operated in a parallel beam position way and embedded with a 1.8 kW Cu K α ceramic X-ray (45 kW), 1 mm wide incident and receiving slits, a 40 mA PIXcel3D 2 x 2 area detector. Samples were prepared for the analysis by precipitating the crude NCs and redispersing them in toluene, the resulting product solution is drop casted on the zero-diffraction silicon substrate and dried at room temperature.

4.3. Compositional analysis.

4.3.a. Inductively Coupled Plasma Atomic Emission Spectroscopy (ICP-AES).

ICP-AES is a spectrographic methodology used to acquire a definite elemental composition of samples; it can also be used for quantitative analysis. ICP-AES works on the principle of, emission of photons from the substance to be measured, that are brought to an excited state using highly energized plasma from an inert gas (usually argon). The atoms which undergo excitation will emit energy at a particular wavelength when their excitons recombine to the ground state followed by the excitation. The wavelength of light emitted is indicative of the presence of particular elements, and the intensity of the spectral signal is indicative of their conc. in the compound.

To determine the concentrations, NCs' samples are often dispersed in a strong acid, following the same to identify the concentration of ionic species is received by elemental analysis.

The basis of performing ICP Mass Spectrometry, or ICP-MS analysis, is based on the ionization of a sample by an extremely hot plasma, and the resulting ions are detected by traditional mass spectroscopy. It has the benefit of being able to measure much lower concentrations of elements present and has also been used to study with unprecedented accuracy and precision the stoichiometry of quantum dot core¹⁰¹.

4.4. Surface chemistry.

4.4.a. Fourier transform infrared (FTIR) spectroscopy.

Fourier-transform infrared (FTIR) spectroscopy is a flexible and prominent way to inspect the NC surface chemistry, providing information about the structure of ligand molecules. NCs whose surface passivation is done using organic ligands such as carboxyl complexes show strong absorption peaks in the span of infrared region, i.e., $3,000\text{ cm}^{-1}$ and $1,500\text{ cm}^{-1}$, which majorly align to the C–H stretching and bending modes and to the carbonyl stretching of surface-bound hydrocarbon molecules. The width and position of infrared resonance recordings can be used to investigate chain identification and order of organic complex capping layer. FTIR also allows for the investigation of the displacement of carbonyl ligands in the case of ligand-exchange reactions¹⁰¹.

4.4.b. Nuclear magnetic resonance (NMR) spectroscopy.

Nuclear magnetic resonance (NMR) spectroscopy is a non-destructive molecular characterization technique that requires minimal entropy of the analysed system, while acquiring the details about the structure and dynamics of molecules at the surface of the colloidal NCs and their surroundings environment. One of the major defects of using NMR spectroscopy to characterize colloidal nanocrystal-ligand complexes is the need for specifically highly concentrated material is needed in order to receive required response when compared to other spectroscopic methods.

Solution - phase ^1H NMR spectroscopy has proven to have excellent potential for in situ identification and quantitative analysis of surface ligands of colloidal nanocrystals, providing structural information on ligand exchange processes and on the adsorption/desorption mechanics of the surface ligands. One of the important pros is that the molecular species confrontation can be observed individually and therefore which can assert us, about the information on its chemical composition. For example, is well known its sensitivity to the difference in chemical environment between free and bounded surface ligands. In particular, the ^1H NMR line width allows to differentiate the bound ligands, which collapse slowly and have broad responses, from ligands moving freely in solution, which display sharp signals. Moreover, ligand shell coverage can be further elucidated using other 2D NMR techniques including diffusion ordered spectroscopy (DOSY), where the resonances of the free and surface-bound ligands can be separated along the diffusion dimension, allowing to

distinguish dynamic ligands in a rapid adsorption/desorption equilibrium, and nuclear Overhauser effect spectroscopy (NOESY), where efficient cross relaxation is indicative of ligand/NC interaction¹⁰².

4.5. Optical characterization.

4.5.a. UV-Vis and NIR spectroscopy.

UV-Vis-NIR spectroscopy is based on the study of the interactions occurring between the examined species, in solution or in solid state, and a beam of energy radiation in the spectral region covering wavelengths from 200 nm to 2500 nm, and it is possible to study transitions occurring among electronic energy levels.

Following the optical absorption processes in the material, the beam passing through the sample will have transmitted intensity $I_T < I_0$ (with I_0 intensity of the light incident on the sample). An absorption spectrum is normally represented as optical transmittance T as a function of the frequency ν , $T(\nu)$ (or wavelength λ , $T(\lambda)$), which is defined as: $T(\nu) = \frac{I_T}{I_0}$.

More often, instead of transmittance, it is used to report a quantity strictly connected to it: Absorbance $A(\nu)$ defined as,

$$A(\nu) = -\log_{10} T(\nu) = \log_{10} \left(\frac{I_0}{I_T} \right), \text{ (equation. 4-2.)}$$

In the case of liquid samples, the absorbance is meant to the concentration of the absorbent species by the Lambert – Beer law: $A(\nu) = \epsilon \cdot b \cdot c$, where ϵ is the molar absorptivity (formerly known as the molar extinction coefficient), which are characteristics of the chemical species undergoing an electronic transition ($L \cdot mol^{-1} \cdot cm^{-1}$), b is the path distance of the sample (cm), and c is the conc. of the compound in the solution ($mol L^{-1}$).

Due to the absorption spectroscopy, it is possible to study the optical properties of nanocrystalline semiconductors. As in the quantum confinement regime, the system generates discrete energy levels in analogy with the problem of the particle in a box/sphere. The optical absorption characteristics of a semiconductor QDs are governed by the energy-level structure of the bound excitons. In the absorption experiment the optically undergoing transitions from the ground state to the various electron–hole pair states are probed. Because of quantum confinement, the absorption (Abs) and photoluminescence (PL) spectra of QDs shift their responses to the blue region upon confinement to a particularly

specific size, when compared to their bulk reference. The sharp absorption features in an Abs. spectrum and narrow peak width of the corresponding PL spectrum can also indicate a nearly monodisperse NCs' sample. For a closely monodisperse sample, the particle concentration in colloidal solution form can be easily calculated by the molar extinction coefficient of the NCs. At wavelengths above 400 nm, well above the first exciton transition, quantum confinement effects are expected to vanish, and the absorption coefficients of colloidal NCs are indeed supposed to be size-independent; this permit to describe light absorption by using bulk molar extinction coefficient and to determine NC concentration in solution, from the absorbance spectrum.

The typical UV-Vis-NIR spectrophotometer contains a monochromator light as source, and a detector. The light source is commonly a deuterium lamp, which emits high intensity ultraviolet radiation; In addition to it, a tungsten lamp, is used as a second source of light, to cover the region in the visible and in the near infrared space of the spectrum. The monochromator, which is a diffraction grating, divides the light beam into its specific wavelengths, and a series of slits which allows the same to concentrate the desired wavelength on the sample cell. The detector is usually a photomultiplier tube, in spite of this in advanced instruments photodiodes are also integrated, while InGaAs detectors are used for applications in the near infrared.

The most common application in UV-Vis-NIR spectrophotometry is the measurement of liquids in cuvettes of a material that is responsive to the electromagnetic radiation which is majorly used in the experiment. A transparent or semi-transparent sample shows various transmission and reflection modes, i.e., it can exhibit transmission, both specular and diffuse, and reflection, both specular and diffuse. The diffuse modes (light scattered in all directions by the sample) arise from particle scattering of the sample and both are typically generated by rough surfaces. All these characteristics are often measured in fractions of the source intensity and depend on the wavelength (λ) or the frequency (ω). The intensity contributions of the reflectance (R), transmittance (T) and absorptance (A) at each wavelength are, according to energy conservation, equal to the intensity of the incident light, which is a unitary term: $1 = T_{(\lambda)} + R_{(\lambda)} + A_{(\lambda)}$. Absorptance is the fraction of light actually absorbed by the sample, determined by accounting for transmission as well as reflectance. Overall transmittance (or reflectance) can mainly be measured by adopting a specific equipment defined as an integrating sphere, which is coated with a barium sulphate. The sample is positioned in front of the sphere or behind and the beam transmitted or reflected by the sample is then collected by the detector by focusing from the integration sphere. The optical

absorption coefficient (α) can be found using the equation: $\alpha(\lambda) = -\frac{1}{d} \ln \left(\frac{T_\lambda}{1-R_\lambda} \right)$, where d is the film thickness^{101,103}.

4.5.b. Photoluminescence (PL) spectroscopy.

An optical method for characterizing, investigating, and detecting point defects or for determining the band gaps of materials is photoluminescence spectroscopy. When doing PL studies, monochromatic laser excitation is used to irradiate the nanocrystal sample (whether it is suspended in a liquid or deposited on a substrate), often with photons with energies exceeding the material's band gap energy, producing an electron-hole pair. Following relaxation, a partly non-radiative and partly radiative emission that is indicative of the nanocrystal or potential defect sites is produced. The Stokes shift refers to the above phenomenon where the optical emission peak for colloidal semiconductor NCs occurs at energies lower than the excitation energy^{101,103}.

5. Synthesis of colloidal SbSBr nanocrystals.

5.1. Materials.

The materials mentioned are with high purity or with the specific concentration mentioned below and they are used as received. Antimony (III) acetate ($\text{Sb}(\text{Ac})_3$ 99.99%, Sigma Aldrich), 1-octadecene ($\text{C}_{18}\text{H}_{36}$ 90%, Alfa Aesar), Oleic acid (RCOOH 90%, Sigma Aldrich), bis(trimethylsilyl)sulfide ($((\text{CH}_3)_3\text{Si})_2\text{S}$ $\geq 98\%$, Sigma Aldrich), Benzyl bromide (BzBr 97%, Acros organics), 1-dodecanethiol (DoSH $\geq 97\%$, Sigma Aldrich), Dodecyldimethylammonium bromide ($(\text{Me}_2\text{Do}_2\text{N}^+\text{S}^-$ $\geq 98\%$ Sigma Aldrich).

The other anhydrous solvents which were used are acetone, toluene, and methanol (technical grade).

5.2. Synthesis procedure.

Colloidal nanocrystals were synthesized in a three neck round bottom flask, which is connected to a Schlenk line setup, which help to avoid oxygen and moisture involvement during the reaction process.

Typical synthesis was carried out in a systematic order primarily with the addition of antimony(III) acetate precursor in a three neck flask with a non-coordinating solvent 1-octadecene and in presence of polar ligand solvent oleic acid (OA), the above mixture was initially stirred well with the help of a magnetic stirrer and the same mixture was heated up to a temperature (temp.) 110°C to dissolve the salts completely and to get a clear solution (sol'n) and in between the heating process, the flask was deaerated and filled with nitrogen gas (N_2) with the help of Schlenk line setup. In a period of one hour the deaeration process was carried-out for three consecutive cycles, which include applying vacuum and N_2 gas purging. Later, the other two anion reagents bis(trimethylsilyl) sulfide ($(\text{Me}_3\text{Si})_2\text{S}$) and Benzyl Bromide (BzBr) were added at 180°C (growth/reaction temperature), under continuous N_2 gas purging and by maintaining the same temp., constant throughout the reaction period of growth i.e., for one hour and after this the flask was cooled down to room temperature normally. The as obtained crude sol'n was centrifuged without any antisolvents, the supernatant was discarded and the left-over pellet was redissolved in nonpolar solvent such as toluene¹⁰⁴. About post synthesis procedures we will discuss in brief in the coming sections of this chapter.

In order of attaining the mono-phase pure colloidal Antimony sulfo-bromide nanocrystals, the kinetic and thermodynamic aspects, time and temperature parameters were altered accordingly and adjusted in such a way to obtain the rod shaped SbSBr NCs.







S.No	Experiment composition ↓	Time (min/hr) →					
		Composition	Instant	5	10	15	30
1	Sb(Ac) ₃ (0.15mmol)- BzBr (0.15 mmol)- TMS(0.15mmol) @180°C						

Table. 5. 1. Colour transition Observation with 0.15 mmol of Sb(Ac)₃ @180°C.

Initially, the reaction was carried out with an assumption of considering one equivalent of 0.15 mmol equally, Antimony (III) acetate (Sb(III)Ac), bis(trimethylsilyl)sulphide (Me₃Si)₂S, and Benzyl bromide (BzBr). During the above reaction the initial observations which were considered, on the formation of SbSBr NCs is yellow¹⁰⁵ colored sol'n, which depict the crystal formation color. The observation for the above reaction is as follows; post dissolution of the salt in 3gm of 1-octadecene solvent in presence of 1.5 mmol OA at 110°C, the mixture was heated to till 180°C and co-injected the (CH₃)₃Si)₂S and BzBr ligand precursors into the flask, during the antimony (III)-oleate complexes react with the injected anion (S²⁻, Br⁻) and the following color transitions were observed, at instant the sol'n turned into a clear yellow sol'n and during this observation the growth temp. is maintained constant i.e., 180°C. Post 15min of S²⁻ and Br⁻ anion injection, nucleation of particles had taken place with an observation of grey substance in the sol'n, and post one hour of the reaction time the particles turned completely into black/grey color, which depicts the formation of **stibnite phase**¹⁰⁶ Sb₂S₃, and later on, the purification of crude sol'n was carried out by centrifuge at 2500rpm for 15 min at room temperature. The supernatant obtained is of reddish clear sol'n, which explains the negligible or no reaction of bromide (Br⁻) with Sb(III)-oleate complex, which made us to control the conc. of the precursors, this explains us about the kinetic and

thermodynamic role in the crystal growth with excess or deficient conc. of precursors availability in the sol'n, which can alter the SbSBr crystal formation and growth¹⁰⁵.

From the above observation, it made us to tune the individual precursor conc., time of growth reaction period, and the reaction temperature. In immediate next sections of this chapter, we will discuss about the effects of crystal growth by varying the conc. of precursor and their respective output.

The typical combination of precursor portion, which yielded the phase pure $Sb_aSb_bBr_c$ are with 0.4 mmol and 0.5 mmol of Sb(III)Ac involvement in the crystal formation. We have considered, these both conditions under two individual cases and compared their crystal formation at different reaction temp. and growth time.

5.2.1. Optimization of Parameters.

5.2.1.1. Optimization of reagents concentration.

Case 1.

In the present synthesis, yielding of SbSBr NCs was considered with the following composition, 0.4 mmol (120mg) of $Sb(Ac)_3$ and 4 mmol of oleic acid (OA), which were added in 3g (≈ 12 mmol) of 1-octadecene. The above mixture was stirred well with the help of magnetic stirrer and deaeration of the flask was done, through the consecutive cycles of vacuum application and N_2 gas purging upto $90^\circ C$. The same mixture was then heated till $110^\circ C$ to dissolve the $Sb(Ac)_3$ salt completely, and appear as colorless and transparent, which explains about the formation of the Sb(III)-oleate complex/es. The sol'n was brought down to $80^\circ C$ and continuous introduction of vacuum is done to eliminate the leftover residue of oleic acid. And the solution was heated up to $180^\circ C$ and stabilized it under the continuous N_2 purging. At this moment, 0.15 mmol (32 μ l) of $(Me_3Si)_2S$ and 0.9 mmol (108 μ l) of BzBr, were added in 2 ml of 1-octadecene, which were co-injected swiftly into the above heated sol'n. The reaction was left to proceed for one hour and in between color transition observations were captured. And later the heating mantel was removed at post one hour of reaction, the obtained crude sol'n was allowed to cool down to the room temperature naturally. Post procedures to the above, the reacted crude product was centrifuged without

any antisolvents at 2500rpm for 15 min, the obtained supernatant was discarded and the pellet remained in the vial is redispersed in anhydrous toluene for the further validation of the synthesized SbSBr NCs for surface chemistry and photo-physics.





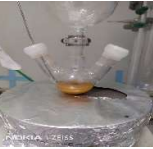

S.No	Experiment composition ↓	Time (min) →					
		Composition	Instant	5	10	15	60
1	Sb(Ac) ₃ (0.4mmol)- BzBr (0.9 mmol)- TMS(0.15mmol) @180°C						

Table. 5. 2. Color transition Observation with 0.4 mmol of Sb(Ac)₃ @180°C.

In the above experiment, the following observations are made, as we co-injected the both precursors at 180°C, at instant the sol'n got changed its color from transparent clear one to the clear yellow, after 5 mins it got transformed into dark orangish color which depicts the amorphous Sb₂S₃¹⁰⁶ substance, later it got transformed into the Sb₂S₃ (stibnite)¹⁰⁶ which could be confirmed with the grey color observation of the particles in the flask. And a topotactic transformation takes place post 15 min. of the reaction. As we have observed that the grey particles have started transforming into yellow particles which explains the formation of the antimony sulfobromide (SbSBr), the validation of the phase formation was done using XRD analysis.

The above composition was analyzed to understand its growth behavior and yield by varying reaction temp. i.e., 130°C, 150°C and 230°C. The following observations were made as, while carrying out the said reactions at mentioned temp., at 130°C we have observed completely an amorphous substance, as for this reason we have neglected the usage of that particular reaction temp. for crystal growth.


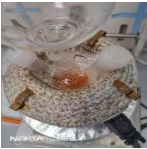


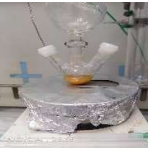

S.No	Experiment composition ↓	Time (min) →					
		Composition	Instant	5	10	15	60
1	Sb(Ac) ₃ (0.4mmol)- BzBr (0.9 mmol)- TMS(0.15mmol) @150°C						

Table. 5. 3. Colour transition Observation with 0.4 mmol of Sb(Ac)₃ @150°C.

At 150°C the observation of the SbSBr NC formation is as follows, the obtained yield is very low when compared to the one synthesized at 180°C. And we have observed the same transformations which we have seen in the above reaction @180°C. So, to avoid the multiple transformations during the reaction procedure and to avoid having multi-phase material, we have decided to analyze the synthesis of SbSBr at another extreme reaction temp. i.e., 230°C.






S.No	Experiment composition ↓	Time (min) →					
		Composition	Instant	5	10	15	60
1	Sb(Ac) ₃ (0.4mmol)- BzBr (0.9 mmol)- TMS(0.15mmol) @230°C						

Table. 5. 4. Colour transition Observation with 0.4 mmol of Sb(Ac)₃ @230°C.

In the present experiment we have introduced the same conc. of the precursors, but we have changed the reaction temp., to observe the yield and the time of SbSBr NCs formation. Unfortunately, we have ended up with the stibnite¹⁰⁶ particles formation on post 15 min of

reaction time. From the above experiment we analyzed that the reaction temp. of 0.4 mmol $\text{Sb}(\text{Ac})_3$ conc. composition is restricted to be maintained at 180°C only.

Case 2.

In the present synthesis, formation of SbSBr NCs was considered with the following composition, 0.5 mmol (150mg) of $\text{Sb}(\text{Ac})_3$ and 4 mmol of oleic acid (OA) were added in 3g (≈ 12 mmol) of 1-octadecene. The above mixture was stirred well with the help of magnetic stirrer and deaeration of the flask was done, through the consecutive cycles of vacuum application and N_2 gas purging at 90°C . The above mixture was then heated till 110°C to dissolve the $\text{Sb}(\text{Ac})_3$ salt completely and appear as colorless and transparent, which explains about the formation of the $\text{Sb}(\text{III})$ -oleate complex/es. The sol'n was brought down to 80°C and continuous vacuum application is done to eliminate the leftover residue of oleic acid. And the solution temp. was raised up to 180°C and stabilized it under the continuous N_2 gas purging. At this moment, 0.15 mmol ($32\mu\text{l}$) of $(\text{Me}_3\text{Si})_2\text{S}$ and 1.2 mmol ($144\mu\text{l}$) of BzBr were added in 2 ml of 1-octadecene, which were co-injected swiftly into the above heated sol'n. The reaction was left to proceed for one hour and in between color transition observations were captured. And later the heating mantle was removed at post one hour of reaction, the obtained crude sol'n was allowed to cool down to the room temperature naturally. Later, the reacted crude product was centrifuged without any antisolvents at 2500rpm for 15 min, the obtained supernatant was discarded and the pellet remained in the vial is redispersed in anhydrous toluene for the further validation of the synthesized SbSBr NCs for surface chemistry and photo-physics.



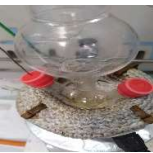



S.No	Experiment composition ↓	Time (min) →					
		Composition	Instant	5	10	15	60
1	$\text{Sb}(\text{Ac})_3(0.5\text{mmol})$ - BzBr (1.2mmol)- $\text{TMS}(0.15\text{mmol})$ @ 180°C						

Table. 5. 5. Colour transition Observation with 0.5 mmol of $\text{Sb}(\text{Ac})_3$ @ 180°C .

From the above experiment with 0.5 mmol $\text{Sb}(\text{Ac})_3$ conc., the observation of NCs formation is as follows, with the above conc. we haven't seen any grey color transition in between, which explains that the $\text{Sb}_2\text{S}_3^{106}$ crystals intermediate phase formation is skipped during the entire reaction period. As the above condition explains us, that the obtained NCs are of mono-phase particles (NCs). And we have proceeded further to analyze the yield and with reaction temp. optimization.





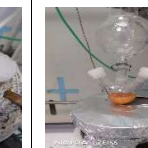
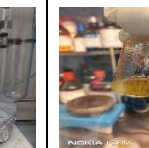
S.No	Experiment composition ↓	Time (min) →					
		Composition	Instant	5	10	15	60
1	$\text{Sb}(\text{Ac})_3(0.5\text{mmol})$ - BzBr (1.2mmol)- $\text{TMS}(0.15\text{mmol})$ @150°C						

Table. 5. 6. Colour transition Observation with 0.5 mmol of $\text{Sb}(\text{Ac})_3$ @150°C.

At 150°C the observation of the SbSBr NC formation is as follows, the obtained yield is high when compared to the one synthesized at 180°C with 0.5mmol $\text{Sb}(\text{Ac})_3$, but with a large portion of amorphous $\text{Sb}_2\text{S}_3^{106}$ substance. And we have observed the same transformations which we have seen in the above reaction i.e., at 180°C (Case 2). So, in order to avoid the multi-phase NCs from the above obtained, we further analyzed the same composition at 230°C.





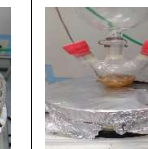
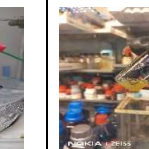
S.No	Experiment composition ↓	Time (min) →					
		Composition	Instant	5	10	15	60
1	$\text{Sb}(\text{Ac})_3(0.5\text{mmol})$ - BzBr (1.2mmol)- $\text{TMS}(0.15\text{mmol})$ @230°C						

Table. 5. 7. Colour transition Observation with 0.5 mmol of $\text{Sb}(\text{Ac})_3$ @230°C.

In the above experiment, the end observations which we have gone through, are no transition to grey substance and the yield output is very low compared to the one which we have obtained at 180°C and 150°C (in Case 2) and moreover when we have compared it with the NCs yield which we have observed with 0.4mmol Sb(Ac)₃ conc. was still low. So, we have finalized the reaction temp. to be 180°C and 0.5 Sb(Ac)₃.







S.No	Experiment composition	Time (min)					
	↓ Composition	Instant	5	10	15	60	RT
1	Sb(Ac) ₃ (0.6mmol)- BzBr (1.5mmol)- TMS(0.15mmol) @180°C						

Table. 5. 8. Color transition Observation with 0.6 mmol of Sb(Ac)₃ @180°C.

To identify the end limits of the SbSBr NCs formation with the above-mentioned reagents, we have inspected till the range 1:10 ratio of Sb₂S₃: SbBr₃ crystal growth reactions. In which we have identified the low yield observation on post reaction procedures and filtration, and no SbSBr crystal formation.

5.2.1.2. Optimization of reaction time.

In order of reducing the reaction time, we have attempted to produce the SbSBr NCs at 15 min. reaction period at 180°C. It is followed upon by; we maintained the reaction composition as same of 0.5mmol Sb(Ac)₃ composition. The current experiment was performed to inspect the yield and its crystal formation and growth, for which we have followed the same procedure which was mentioned earlier in this chapter in order to obtain the SbSBr NCs, unfortunately we couldn't obtain, high yield SbSBr NCs in 15 min. as in the current experiment we haven't introduced any growth terminating agents in the reaction chamber, in attaining single phase SbSBr NCs at 15 min.



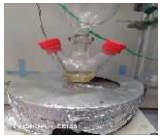

S.No	Experiment composition ↓	Time (min) →					
		Instant	5	10	15	60	RT
1	Sb(Ac) ₃ (0.5mmol)- BzBr (1.2mmol)- TMS(0.15mmol) @180°C						

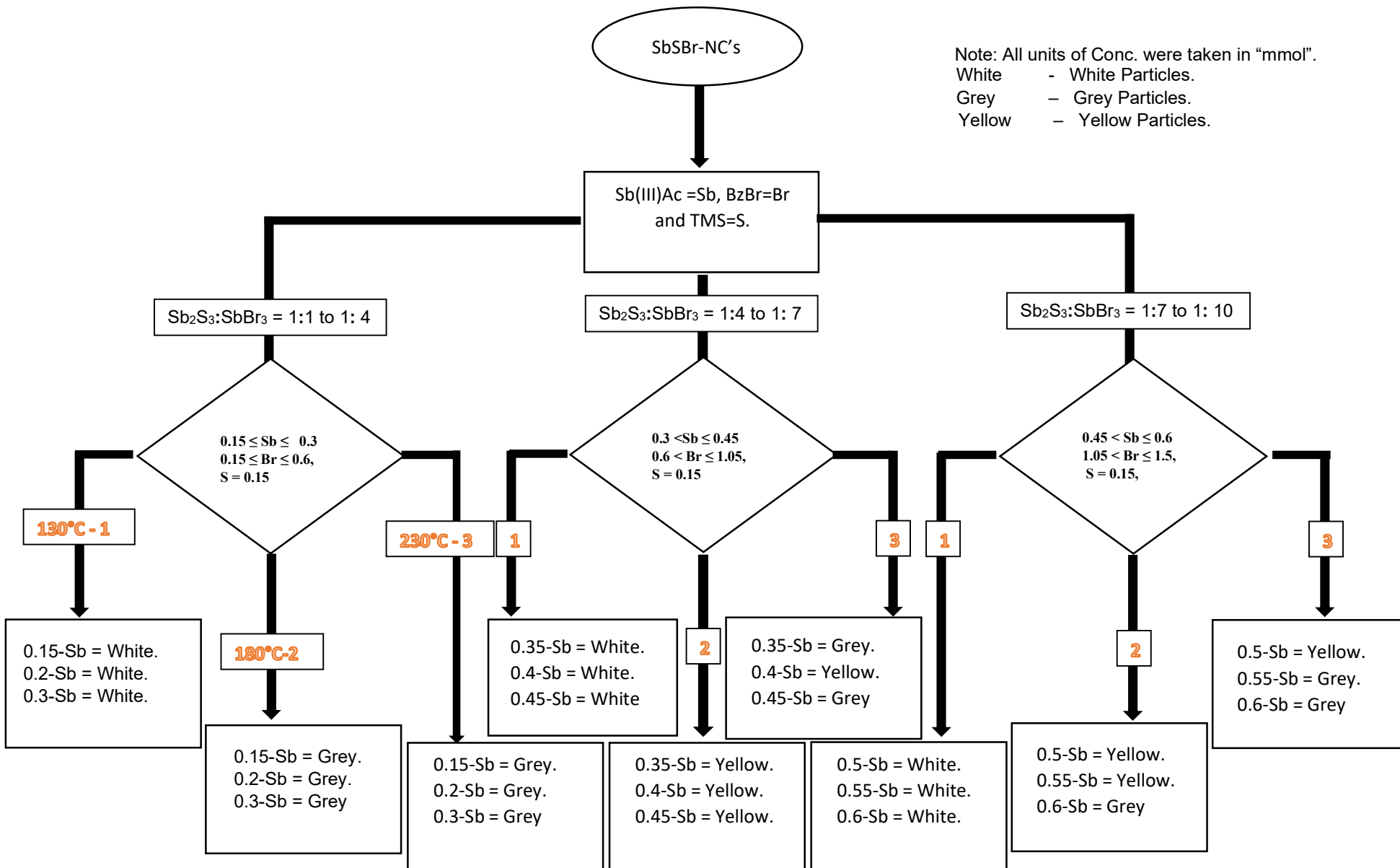
Table. 5. 9. Colour transition Observation with 0.5 mmol of Sb(Ac)₃ @180°C- 15min.

During the above experiment the observations which we have seen was very low or negligible amount of yield.

To the end, after going through multiple observations by varying the aspects, such as: precursor concentration, temperature and reaction time, we have finalized the optimal conditions for the growth and the reaction period of, 0.4 mmol and 0.5 mmol of Sb(Ac)₃ conc. at 180°C for a period of one hour of reaction time. The validation of the cleaned SbSBr NCs was done with the respective characterization works, which details about the surface chemistry and the photo-physics of the obtained NCs at the respective growth conditions.



Fig. 5. 1. a, b, and c, are the images of as-synthesized SbSBr NCs.



Flow Chart. 1. Schematic representation of the Optimization of the synthesis processes.

5.3. Results and Discussion.

5.3.1. Morphological, Structural, and Optical Characterization.

a. Morphological analysis.

From the above synthesis section, post co-injection of the S and Br precursors to the Sb-oleate sol'n at 180°C, the yellow precipitate obtained was inspected with the help of TEM instrument. The TEM inspection revealed about the formation of rod like NCs (fig. 5.2. d), with the following dimensions, with length $\approx 6\mu\text{m}$ and width $\approx 100\text{nm}$ with a promise of polydispersity availability in the sample (fig.5.2.f, g).

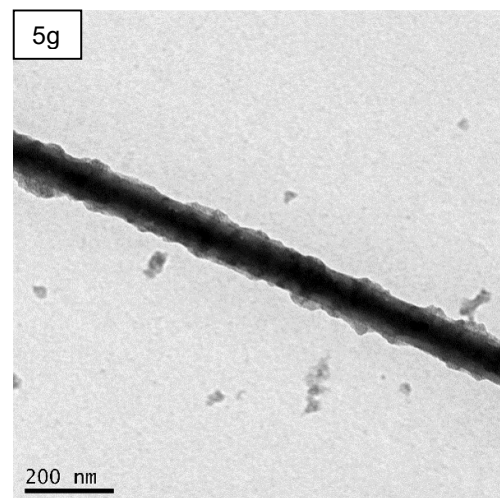
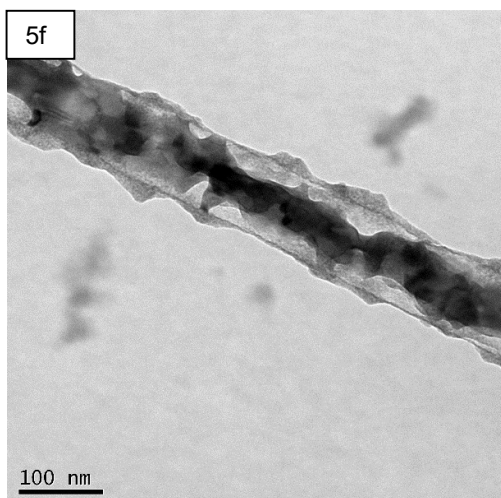
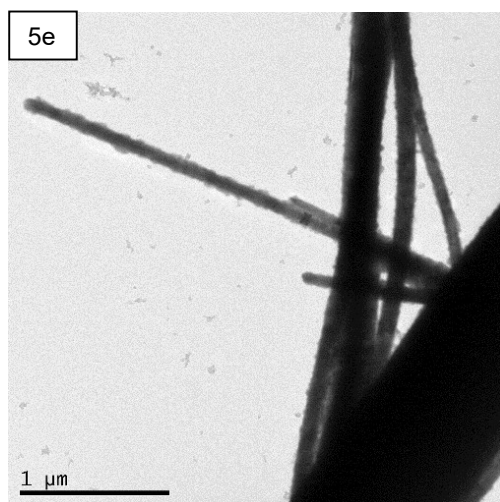
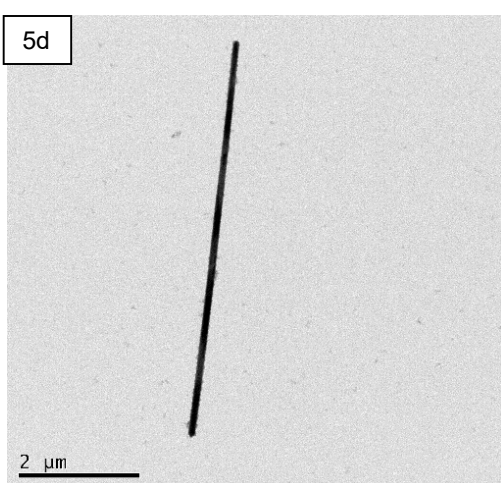


Fig. 5. 2. d, e, f, and g, are TEM images of as-synthesized 0.4-SbSBr-180°C NCs.

Through the above TEM inspection, it made clear to us that the growth of the NCs is purely based on the expense of small particles in the sol'n, which can be cross-interpreted with the help of LaMer mechanism⁴ and Ostwald ripening⁹⁵ conditions.

From the above fig. 5.2., we have clearly understood the growth mechanism i.e., SbBr_3 are being attracted towards the in-growth crystals and that too are being under the vicinity of its critical radius, the crystal grows further in the absence of the growth terminating agents in the reaction mixture/sol'n.

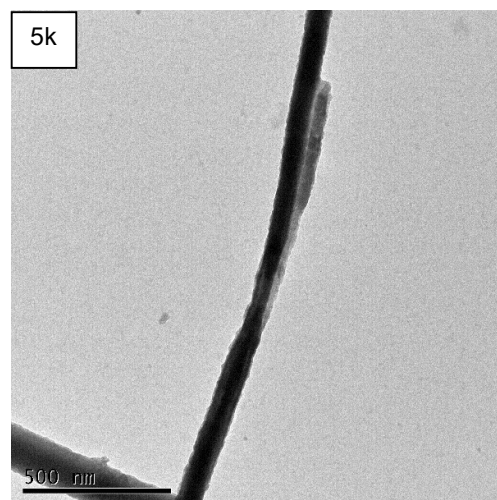
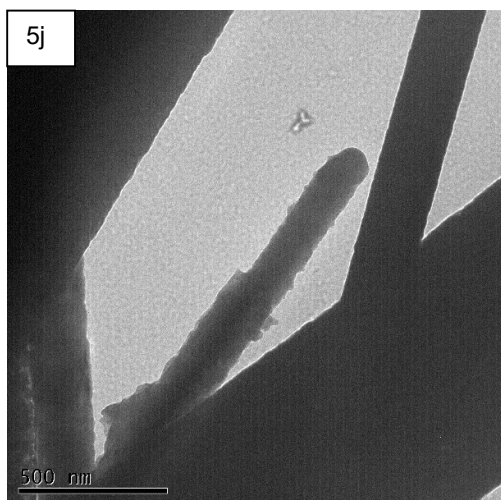
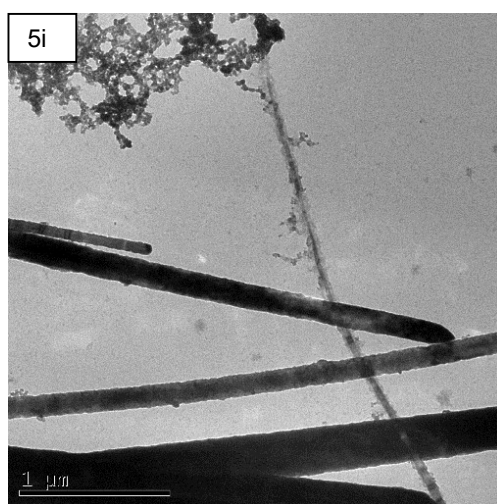
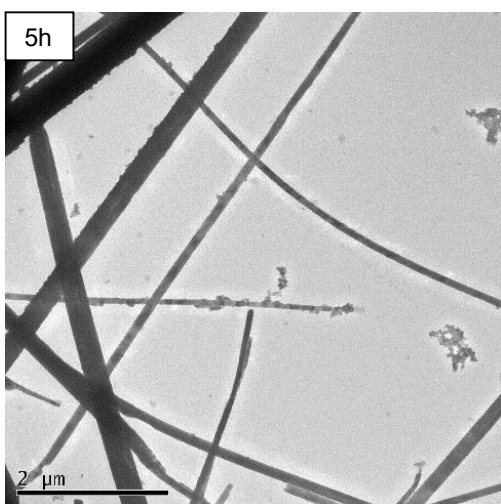


Fig. 5. 3. h, i, j, and k, are TEM images of as-synthesized 0.5-SbSBr-180°C NCs

In the present fig. 5.3., with 0.5mmol $\text{Sb}(\text{Ac})_3$ conc. at 180°C the crystal mixture (post cleaning) are with negligible or near detectable portion of amorphous Sb_2S_3 ¹⁰⁵ substance in the sol'n, which can be filtered with the help of regular precipitation/size selective precipitation.

Most of the works which were reported till date, about the SbSBr NCs were attained through the solid state reaction methods. As from the literature, it was mentioned that the SbSBr NCs were disintegrated post formation of the compound, and some of the reports stated about the split/rupture of the NCs edges¹⁰⁷. In our works, we have achieved a clear rod like NCs with no visible structural defects. The above NCs were with the dimensions are as follows, length $\approx 6\mu\text{m}$, and width $\leq 100\text{nm}$, with a polydispersity index in size magnitude.

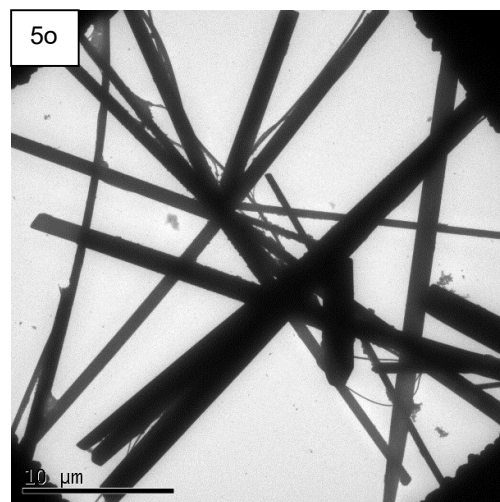
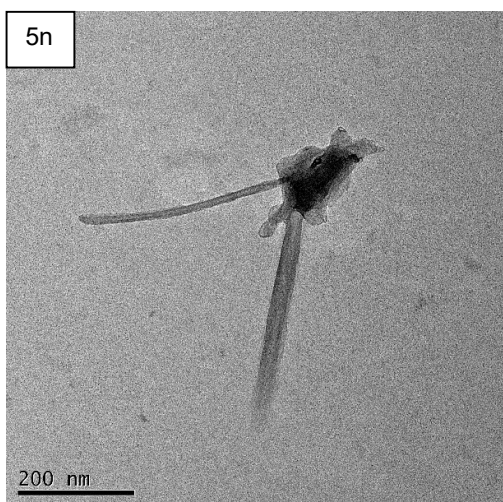
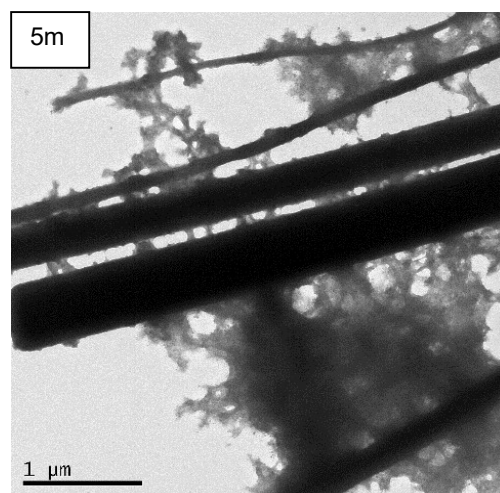
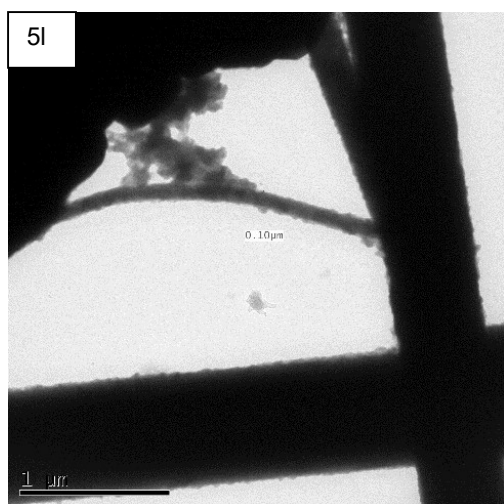


Fig. 5. 4. l, m, n, and o, are TEM images of as-synthesized 0.5-SbSBr-150°C NCs.

During the above analysis period on 0.5mmol Sb(Ac)₃ at 150°C, we have observed that the NCs grown are of with higher aspect ratio than compared to the 0.4mmol Sb(Ac)₃ and 0.5mmol Sb(Ac)₃ both at 180°C. Moreover, with the mentioned conc. we haven't observed any split/rupture of the NC edges, which made us to further analyze the present composition with the same growth parameters but with a reduction of reaction temperature i.e., at 150°C.

The obtained crystals are with rod like structures, the observed dimensions of the NCs at 150°C, are length ≈6μm, and width ≥100nm. There were no significant morphological changes observed, even upon varying the reaction temperature.

b. Structural analysis.

In order of validation of the obtained XPD pattern, we have performed curve refinement and fitting using GSAS-II software, upon attribution of the obtained data with the existing crystal structure using QualX 2.0 i.e., orthorhombic structure with Pnma/62 space group, and a crystal phase match was attained with the following JCPDS card n^o. 00-231-0798⁹. In addition, it made us clear that no other phase group is in existence of the synthesized SbSBr metamaterial.

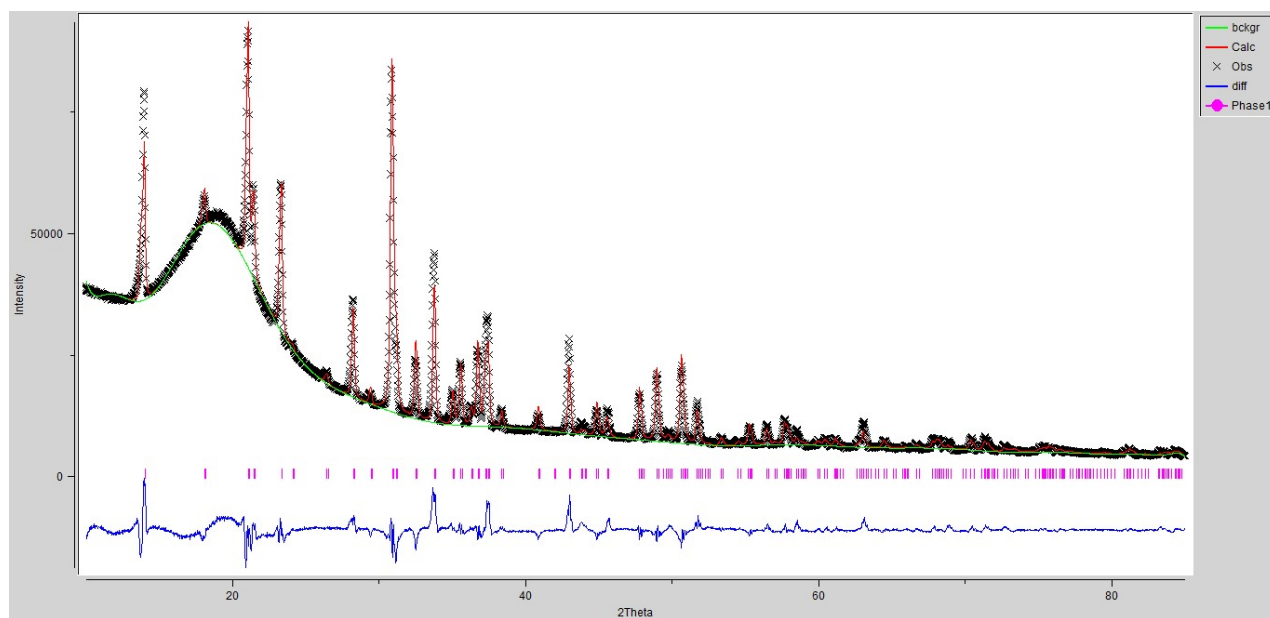


Fig. 5. 5. Refinement fit obtained on the data obtained with 0.4mmol Sb(Ac)₃ conc. at 180°C⁷.

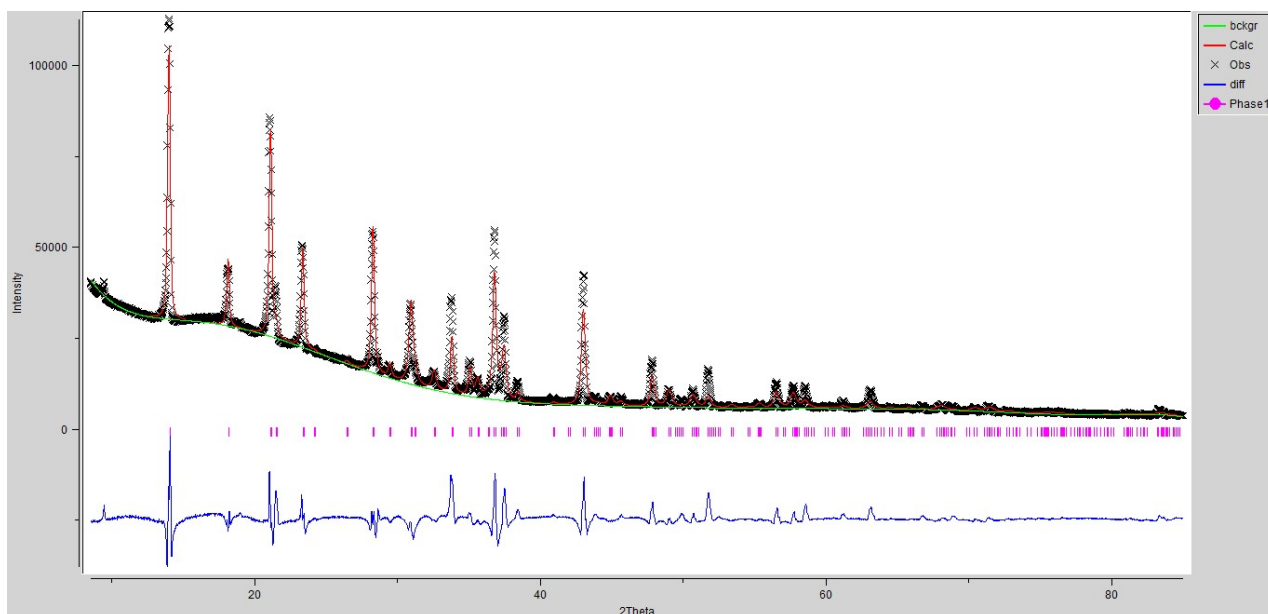


Fig. 5. 6. Refinement fit obtained on the data obtained with 0.5mmol Sb(Ac)3 conc. at 180°C7.

In order to calculate the crystal lattice and atomic positions of a unit cell, the refinement was carried out, with the help of GSAS-II by taking the reference PDF-2 (JCPDS)^{9,10}. The obtained lattice parameters of a crystal are mentioned below with the variation undergone in reference to the JCPDS card database.

Lattice parameter	JCPDS card n ^o . 00-231-0798.	Obtained XPD data	Variation %
a.	8.2600 Å	8.3023 Å	0.51
b.	9.7900 Å	9.7790 Å	0.112
c.	3.9700 Å	3.94006 Å	0.754

Table. 5. 10. Observation of the variation obtained in the synthesized 0.5-SbSBr-180°C lattice parameters.

The shift in 2θ and intensity of the XPD pattern, was observed along with the change in the conc. and reaction temperature. The high intensity peak was recorded in PDF-2 database is at 30.93° (2θ)⁹, when it comes to the 0.4mmol $\text{Sb}(\text{Ac})_3$ Conc. NCs had exposed a high intensity peak at 30.78° (2θ), in the case with 0.5mmol $\text{Sb}(\text{Ac})_3$ Conc. at 30.85° (2θ), the intensity counts was not maximum, and significantly with the same 0.5mmol $\text{Sb}(\text{Ac})_3$ Conc. with reaction temperature 150°C , the high intensity peak was observed at 30.88° (2θ). In this way we have understood that the unit lattice constants and atomic positions of a unit cell are varied with respect to the Conc. and accreditation temp.

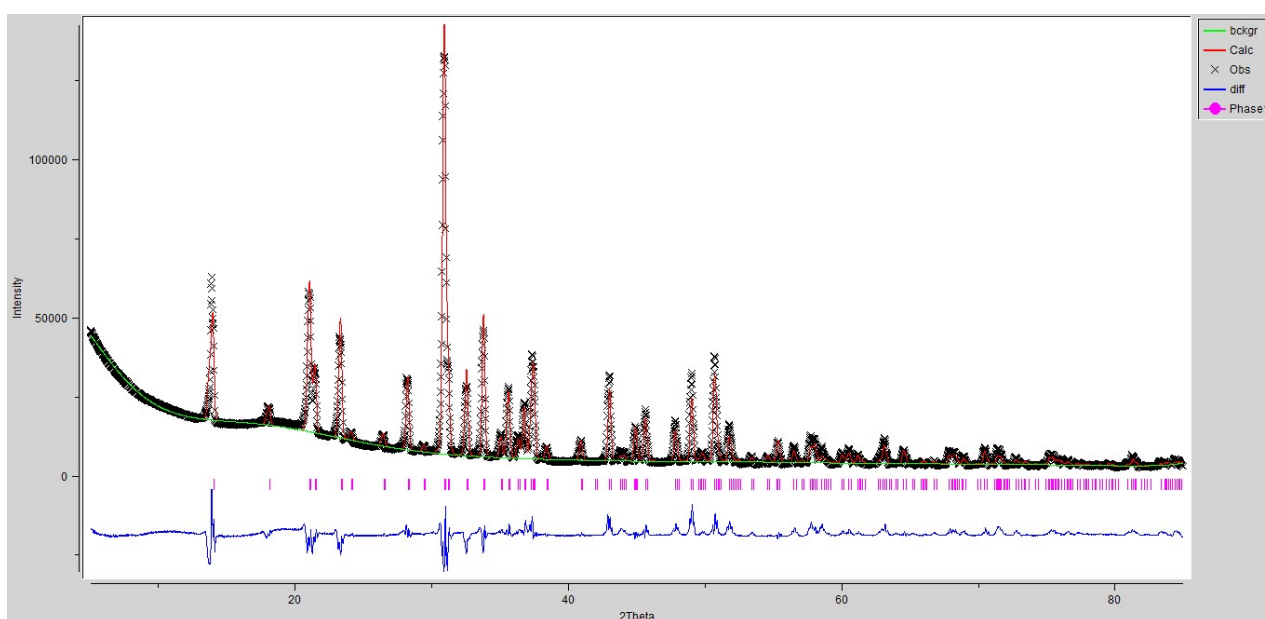


Fig. 5.7. Refinement fit obtained on the data obtained with 0.5mmol $\text{Sb}(\text{Ac})_3$ conc. at 150°C .

In result we have identified the crystal structure of our NCs, with the help of XPD and TEM analysis. As the mono-dimensional NCs were extended in c-axis, with a constrain in the other two directions in cartesian co-ordinate system. The formation of NCs was observed to be in layer form, with a covalent nature in between the layers. The total n°. of elements occupied in a unit cell were 12, (Sb-4, S-4, and Br-4). The pictorial representation of the unit cell of the NCs, were drafted below in reference to the experimental data obtained through the XPD pattern *fig 5.6*.

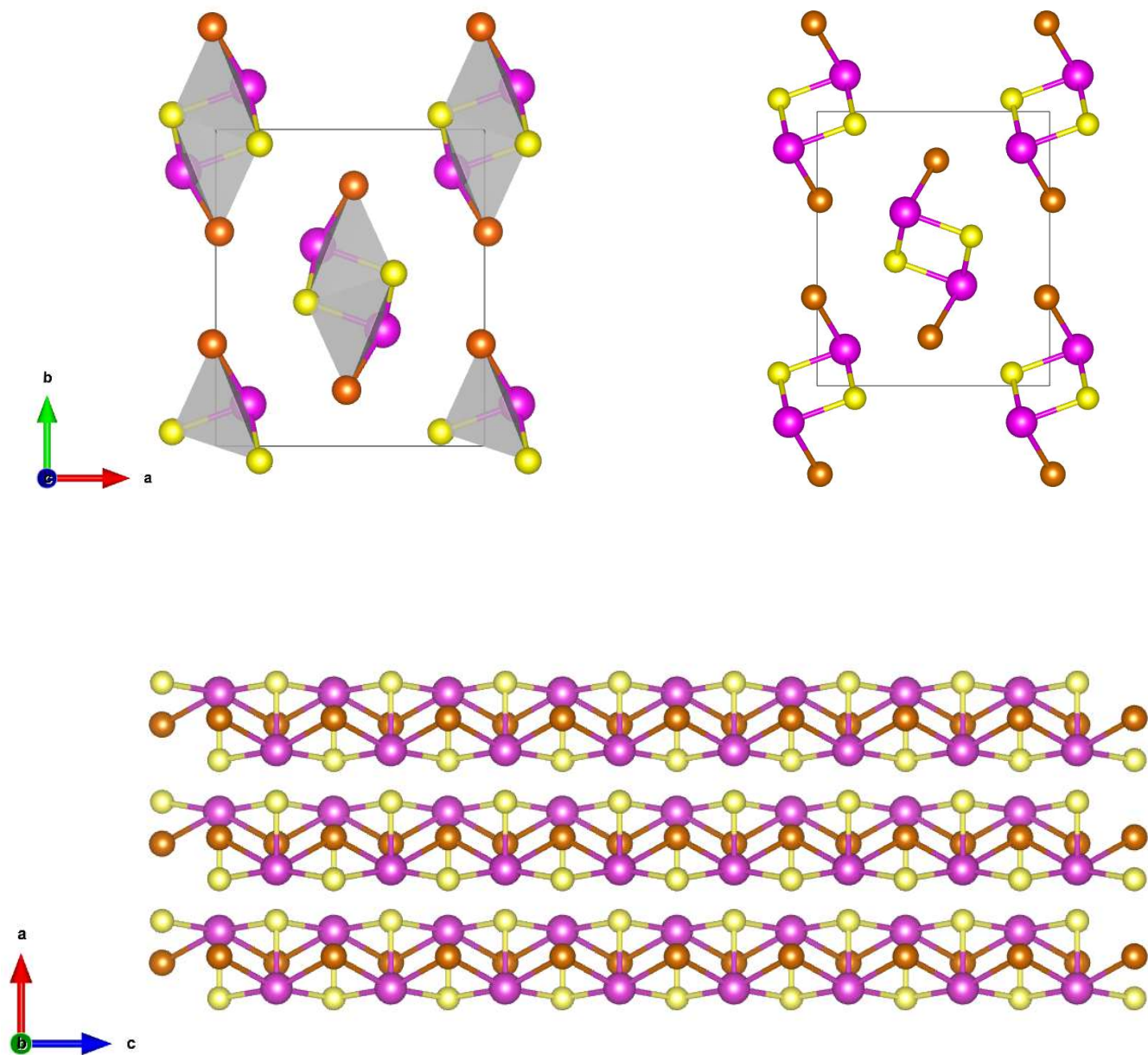


Fig. 5. 8. Post refinement, computed crystallographic data obtained on 0.5mmol $\text{Sb}(\text{Ac})_3$ conc. at 180°C , Sb-pink, S-yellow, and Br-brown⁸.

The below fig.5.9., was plotted with an offset intensity condition, in order to undergo the observation of intensity match variation of the XPD pattern and the peak position in 2θ range. It was clear that the peaks match at particular 2θ point, are varied with the magnitude of intensity.

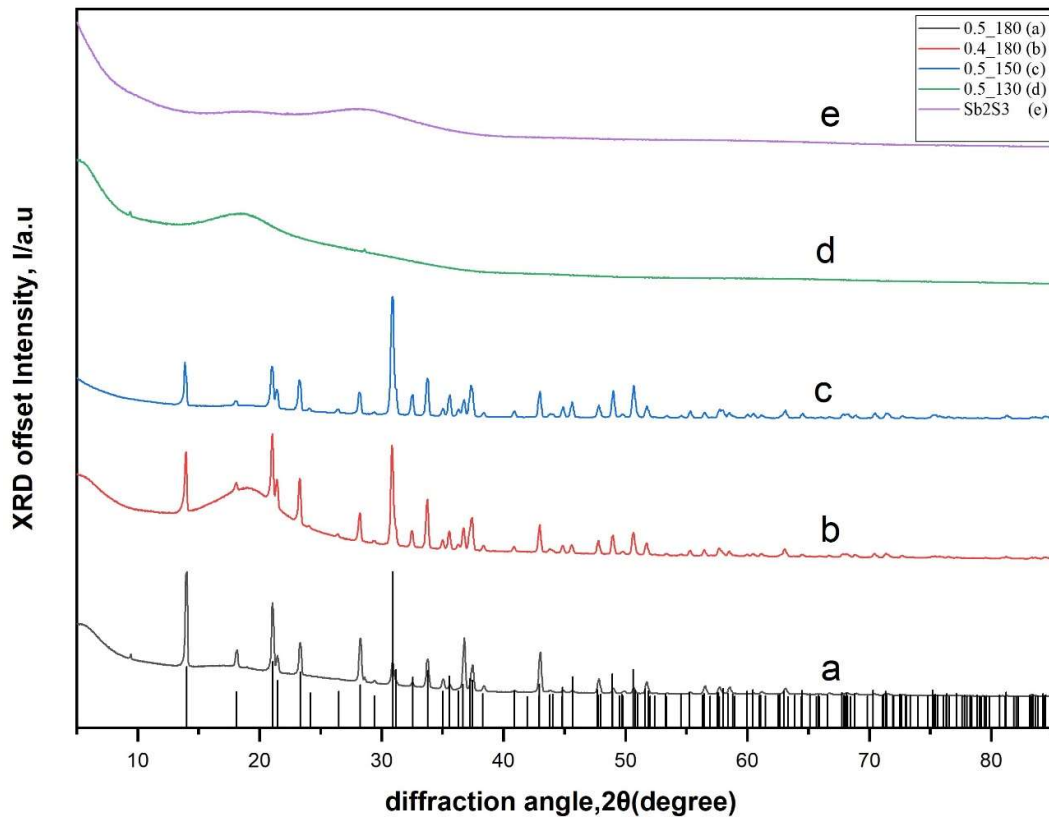


Fig. 5. 9. The offset intensity patterns of XPD data of 0.5-SbSBr at 180°C, 0.4-SbSBr at 180°C, 0.5-SbSBr at 150°C, 0.5-SbSBr at 130°C, and Sb₂S₃ NCs at 180°C^{9,10}.

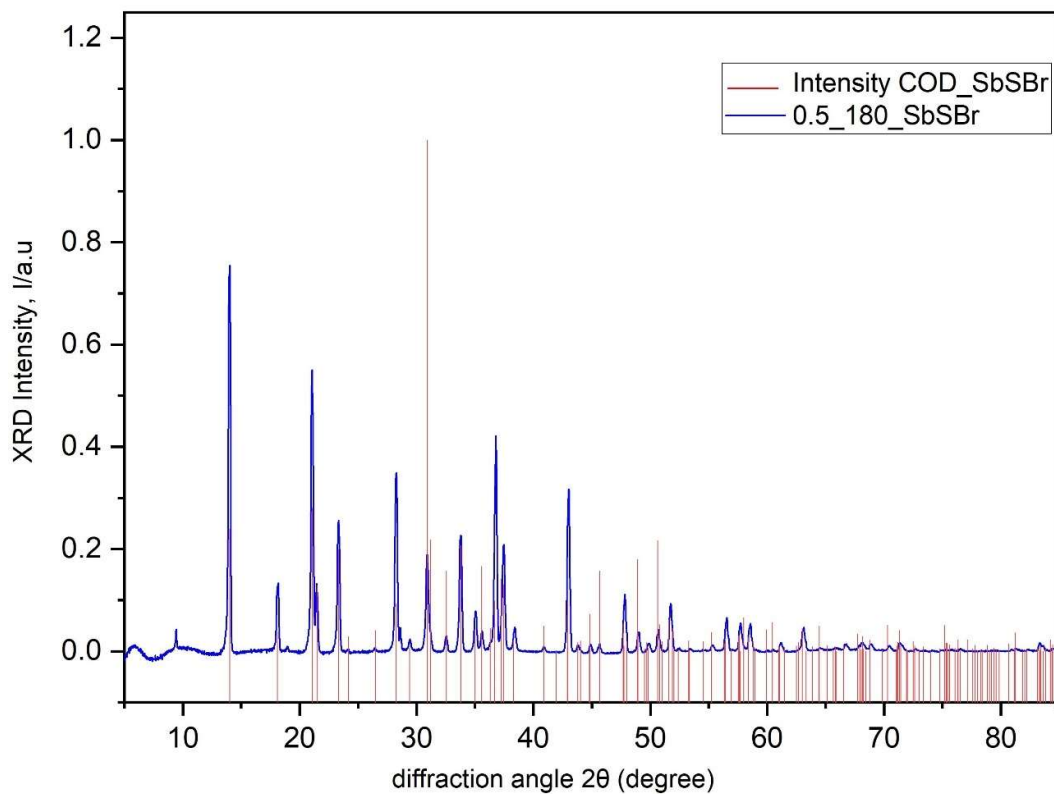


Fig. 5. 10. XRD pattern of 0.5-SbSBr at 180°C with the cross reference of 00-231-0798^{9,10}.

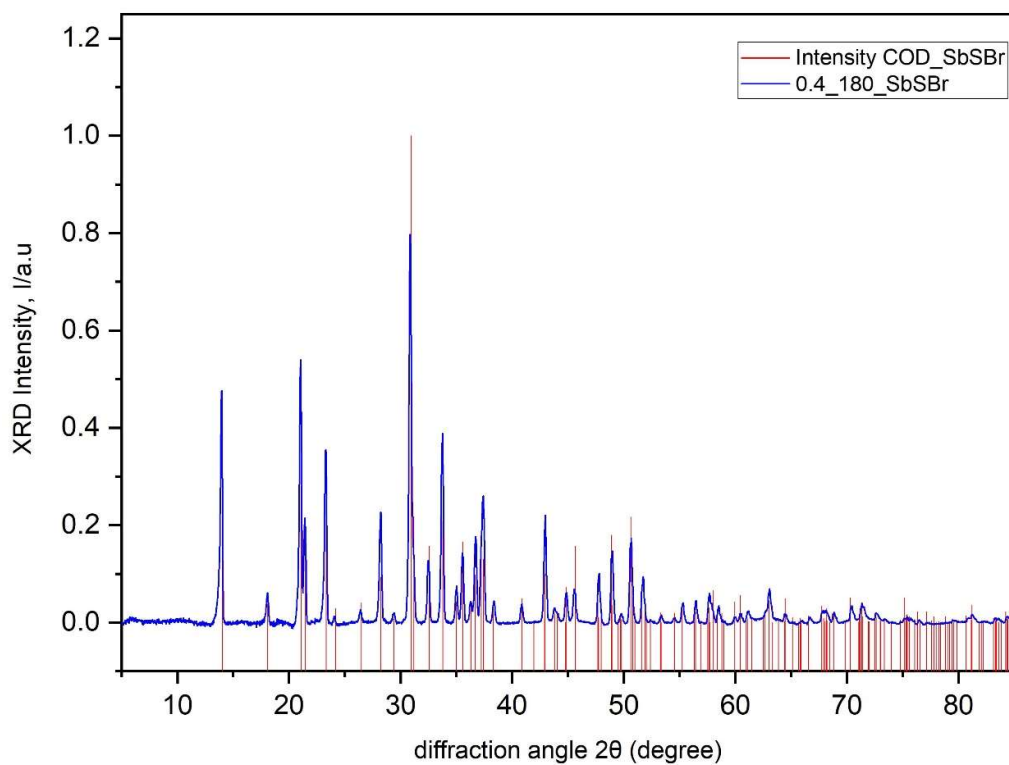


Fig. 5. 11. XRD pattern of 0.4-SbSBr at 180°C with the cross reference of 00-231-0798^{9,10}.

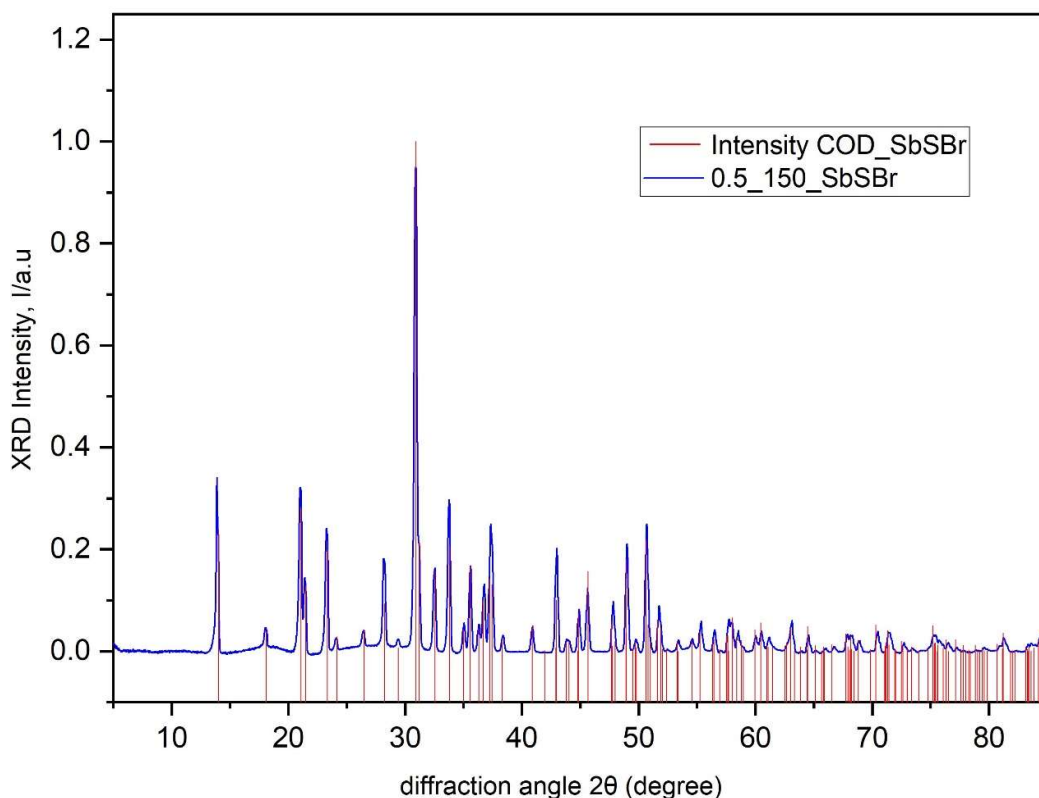


Fig. 5. 12. XRD pattern of 0.5-SbSBr at 150°C with the cross reference of 00-231-0798^{9,10}.

c. Optical characterization.

Colloidal SbSBr NCs have shown an efficient optical property i.e., absorption coefficient α in the range of encouragement, when in comparison to other lead-based chalcogenide and halide PV materials it is an acceptable one, for approach. In order to execute the optical properties on our metamaterial, we have dispersed the sample in toluene, in order to undergo the absorption and scattering upon the incident of light. The obtained absorption spectra were used to estimate the NC indirect band gap, which is 1.80eV (0.5-SbSBr at 180°C). The direct band gap is expected to be near close to the indirect band gap, which was 2.18eV (0.5-SbSBr at 180°C).

It was observed that as we increase the halide Conc., the energy gap between the two levels decreases, and the range of absorption conditions also varies accordingly.

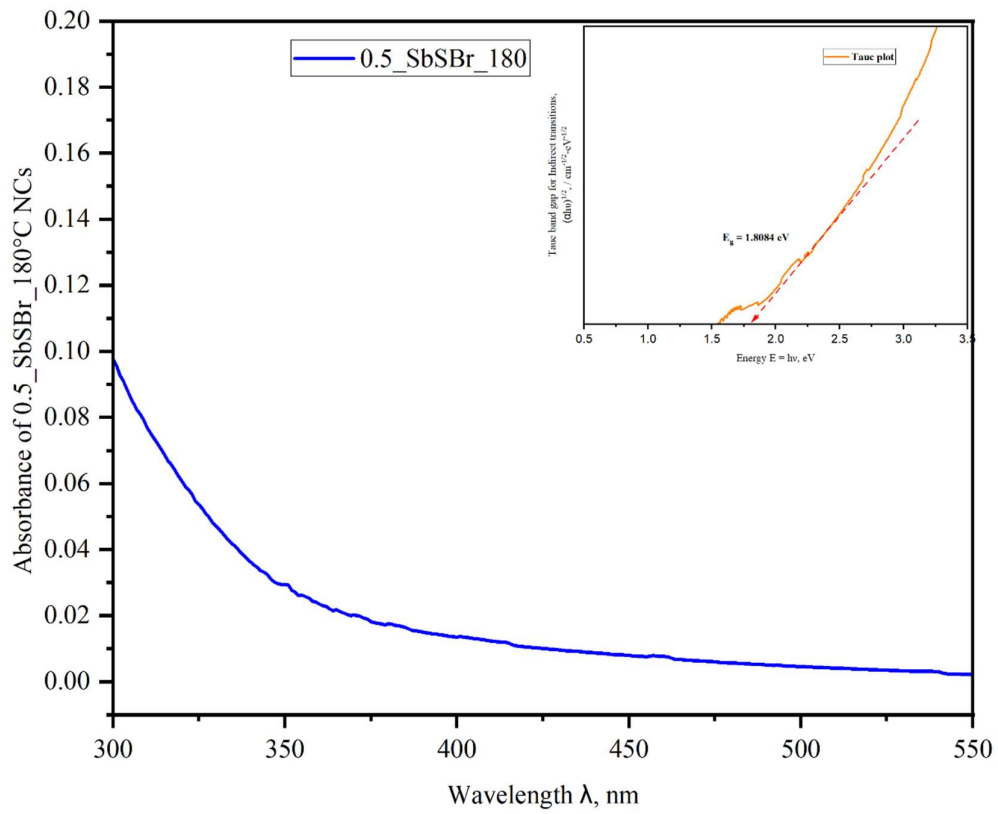


Fig. 5.13. Absorbance of 0.5-SbSBr at 180°C with band gap using the Tauc plot⁹.

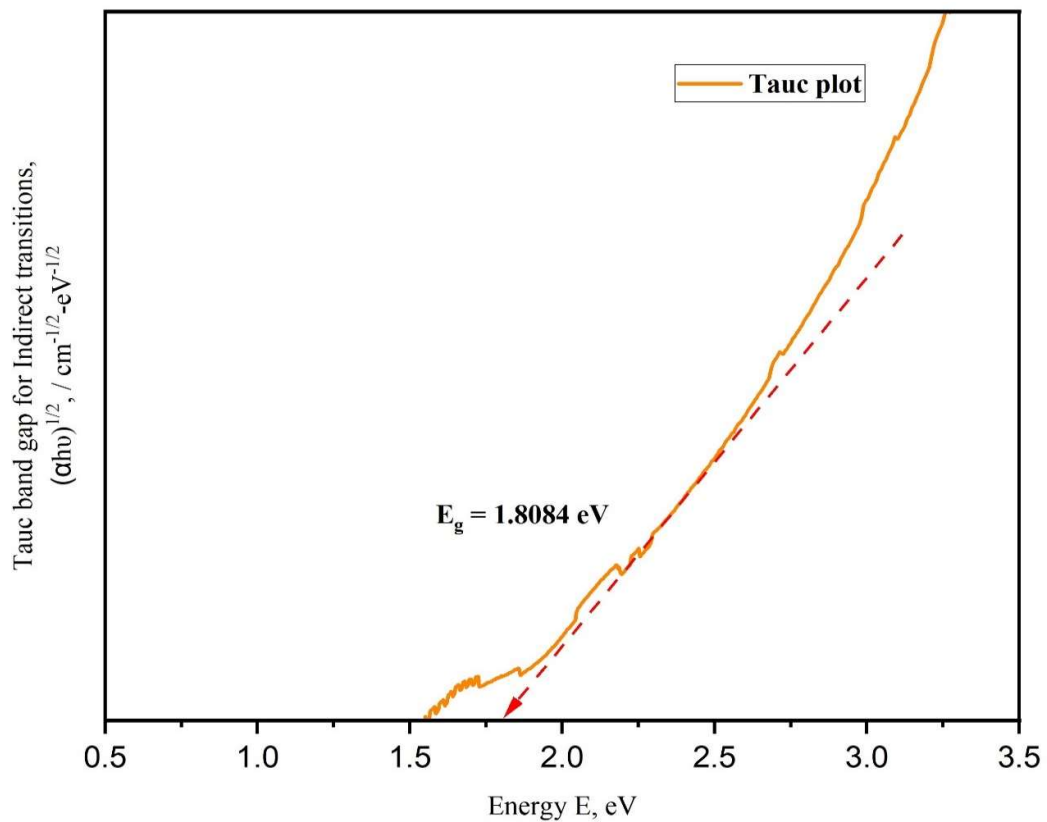


Fig. 5.14. Tauc plot for indirect transitions for 0.5-SbSBr at 180°C.

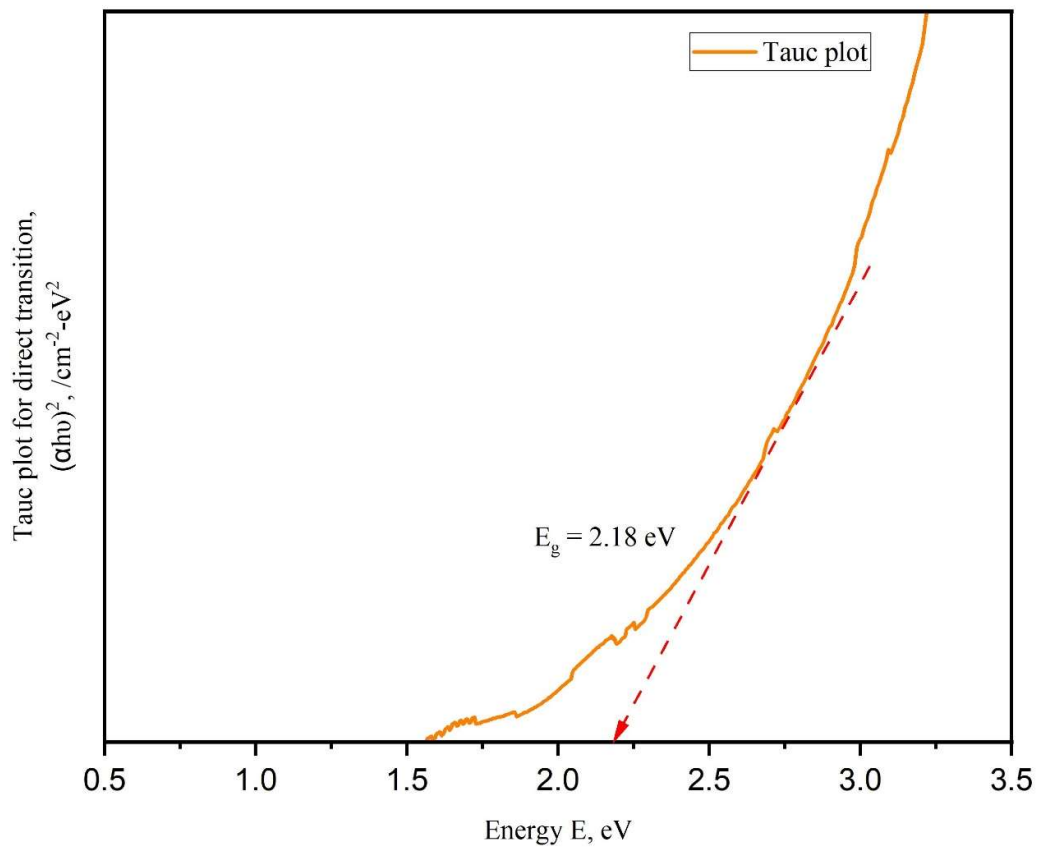


Fig. 5. 15. Tauc plot for direct transitions for 0.5-SbSBr at 180°C.

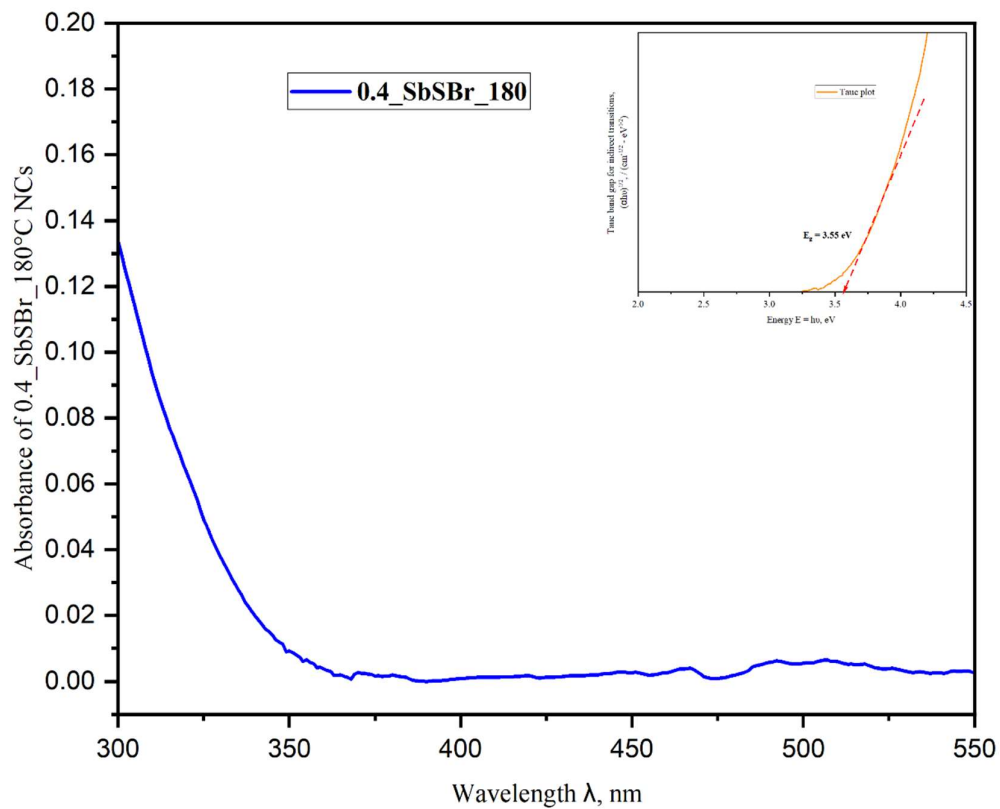


Fig. 5. 16. Absorbance of 0.4-SbSBr at 180°C with band gap using the Tauc plot⁹.

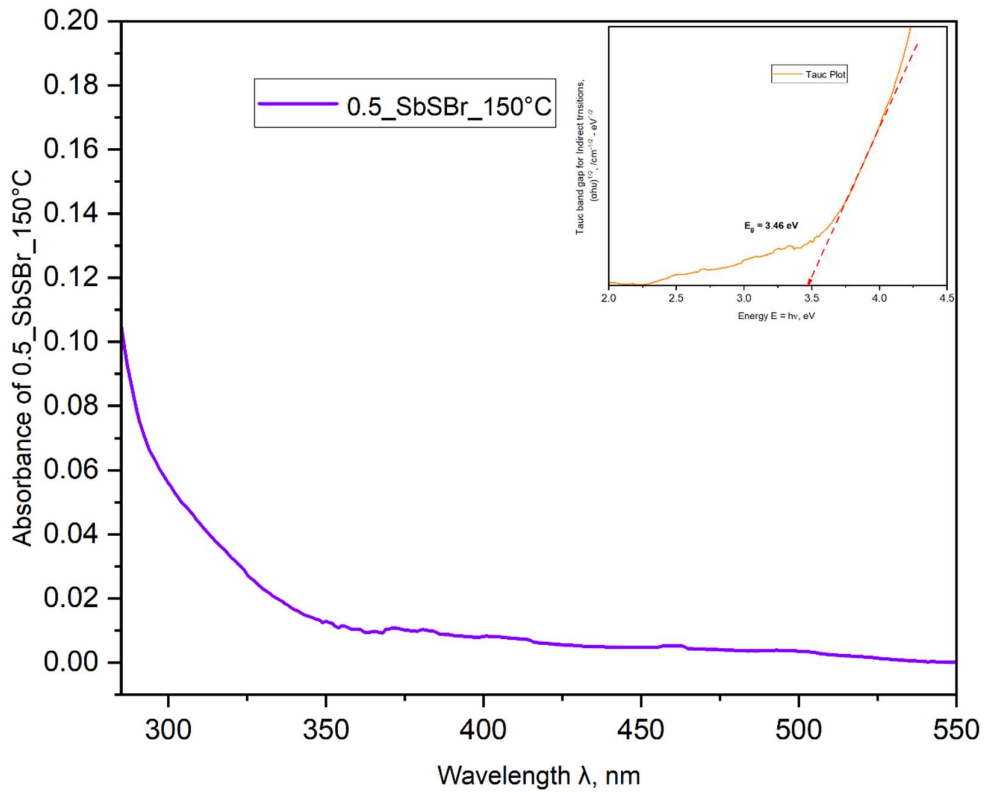


Fig. 5.17. Absorbance of 0.5-SbSBr at 150°C with band gap using the Tauc plot⁹

d. Theoretical calculations.

DFT calculations were performed by using Quantum espresso-Burai (GUI), for the estimation and validation of the band gap and mode of transition i.e., indirect band transition. Moreover the present analysis had revealed that, most of the bands involved in transition on either side of the energy levels are localized on S and Sb atoms respectively. The obtained bands are reproduced qualitatively with the help of experimental data obtained in the various stages of characterization works.

The variation in band gap was observed with respect to the experimentally obtained one i.e., 1.8018eV to 1.7667eV, difference observed is 300meV.

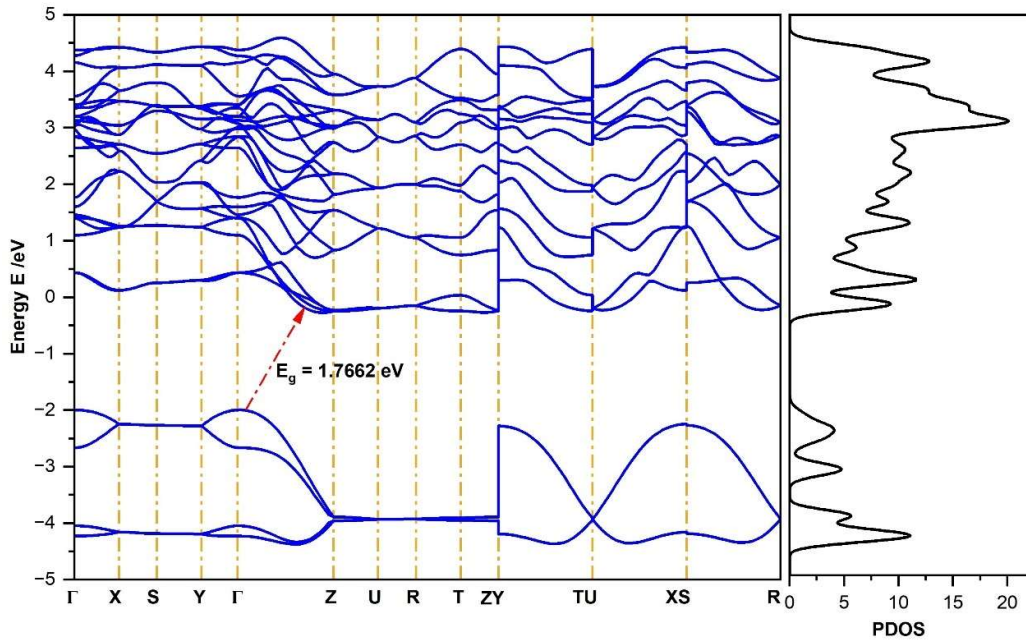


Fig. 5.18. Computed band gap structure and density of states of SbSBr, along with the PDOS^{9,10}.

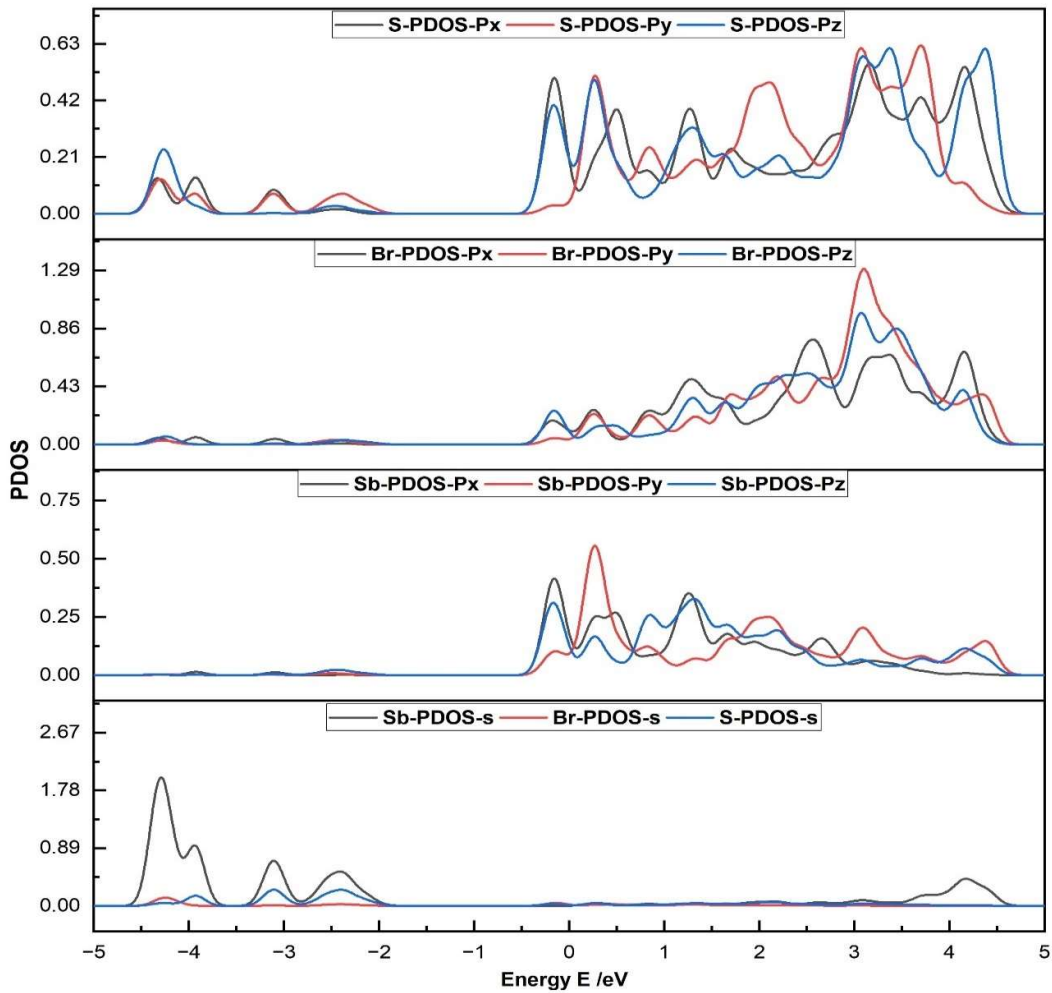


Fig. 5.19. Computed energy levels of atomic orbitals of 0.5-SbSBr at 180°C.

e. Stability and surface chemistry of SbSBr NCs.

The as-synthesized SbSBr NCs, having Sb as major element of composition, explained us that their surfaces may be terminated with the oleate complexes, in-addition the intactness of the NCs structure to the surroundings, cleared us about its stability. We have performed an IR transmission analysis, to identify the surface elements/agents.

At 3000 cm^{-1} we have observed a C-H stretching peak, at 1700 cm^{-1} and at 1400 cm^{-1} , we have observed other peaks related to the stretching energy levels of C=O. As the prominence of the availability of the above defined stretching peaks in the FTIR analysis, had clarified about the availability of the surface ligands over the grown NCs.

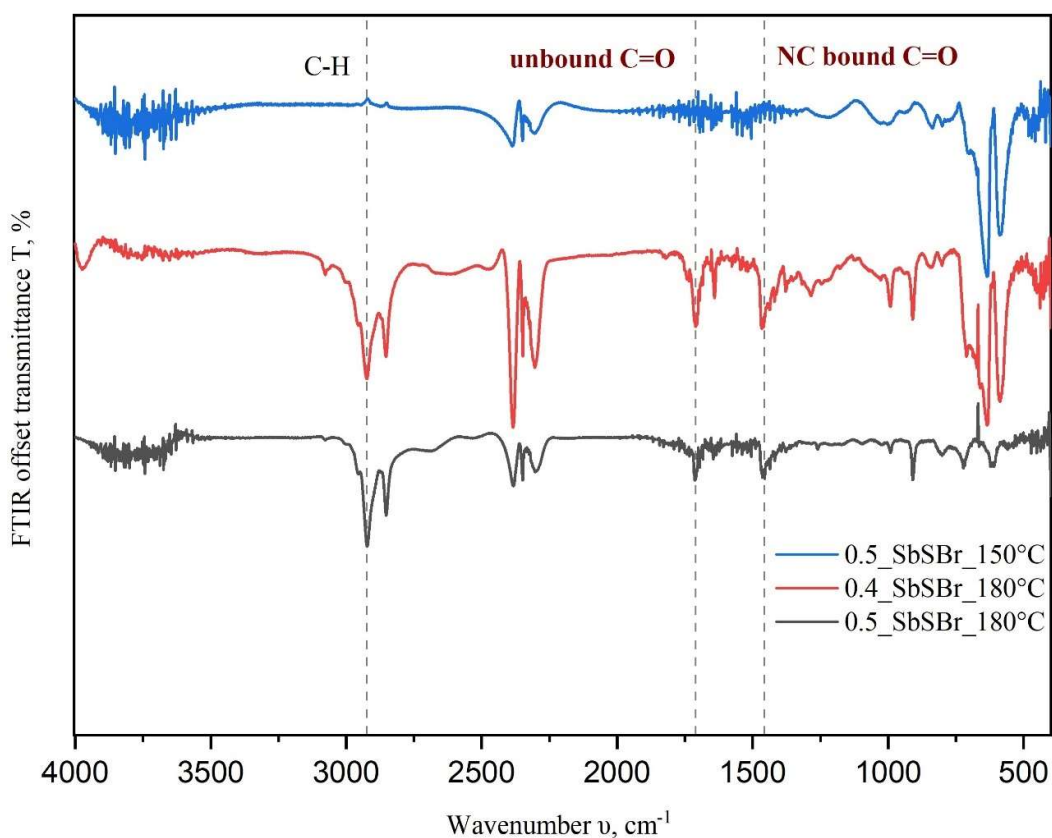


Fig. 5.20. FTIR spectra of 0.5-SbSBr NCs at $180^\circ C$, capped with oleic acid.

6. Conclusion.

The development of nontoxic, stable and defect tolerant inorganic semiconductor nanomaterials lead us to investigate the Antimony chalcogenide NCs development, upon achieving promising results in the synthesis and characterization of antimony chalcogenide NCs. Regarding future applications, these results revealed about the potential of $Sb_aS_bBr_c$ NC thin films as an alternative solar energy conversion material and may stimulate further investigation towards application in photocatalysis and photodetectors. Furthermore, this synthetic approach may encourage the exploration of other metal chalcogenides, as a group of materials that at today's date were vastly unexplored completely at the nanoscale.

Since, the initial discovery of colloidal inorganic semiconductor NCs, most of the research interest/works were focused on their remarkable properties, including high photoluminescence quantum yields, defect tolerance, comparatively to the above very few works were reported, on the importance of the surface chemistry of these material, at the level of physical and chemical processes.

In our synthetic approach, we have developed a stable SbSBr NCs, within the range of nano scale. The approach towards these non-toxic NCs were validated by performing, morphological, structural and photo-physics analysis and to the end surface chemistry of the SbSBr NCs was done. And the results which we have obtained were in an acceptable range of various applications such as, photovoltaics, photocatalysts and photo-electrochemistry. Moreover, the large optical band absorption coefficients in the range of visible spectrum range, made these metamaterials as prominent solar absorbers¹⁰⁷. In addition to the above, the stable condition of the NCs in ambient condition, revealed about their integration into various device electronics.

To the further extent, the current nanocrystals (NCs) can be confined to a particular range of dimensional magnitude, by introducing the growth terminating and size-shape controlling agents in the reaction mixture, which is an un-explored part in the current thesis work, which requires further investigations to carry out.

Further validation and investigation of SbSBr NCs were not performed due to time constrain, which will be addressed soon on another platform.

7. References.

1. Krauss, T. D. & Peterson, J. J. Electronic structure and optical transitions in colloidal semiconductor nanocrystals. in *Colloidal Quantum Dot Optoelectronics and Photovoltaics* vol. 9780521198264 59–86 (Cambridge University Press, 2010).
2. Donegá, C. de M. Synthesis and properties of colloidal heteronanocrystals. *Chem. Soc. Rev.* **40**, 1512–1546 (2011).
3. Books Received. *Science (1979)* **206**, 442–490 (1979).
4. LaMer, V. K. & Dinegar, R. H. Theory, Production and Mechanism of Formation of Monodispersed Hydrosols. *J Am Chem Soc* **72**, 4847–4854 (1950).
5. Egerton, R. F. *Physical Principles of Electron Microscopy*. (Springer US, 2005). doi:10.1007/b136495.
6. Yanai, J., Tanaka, S., Nakao, A. & Abe, S. Materials and Methods. in *Changes in Paddy Soil Fertility in Tropical Asia under Green Revolution* 13–16 (Springer Nature Singapore, 2022). doi:10.1007/978-981-16-5425-1_2.
7. Toby, B. H. & Von Dreele, R. B. *GSAS-II* : the genesis of a modern open-source all purpose crystallography software package. *J Appl Crystallogr* **46**, 544–549 (2013).
8. Momma, K. & Izumi, F. *VESTA 3* for three-dimensional visualization of crystal, volumetric and morphology data. *J Appl Crystallogr* **44**, 1272–1276 (2011).
9. G.D. Christofferson and J.D. McCullough. The crystal structure of antimony(iii) sulfobromide, sb s br. *Acta Crystallographica* **12**, 14–16 (1959).
10. T. Inushima and K. Uchinokura. X-ray structural analysis of ferroelectric antimony sulfobromide. *Jpn J Appl Phys* **24**, 600–602 (1985).
11. Yin, Y. & Alivisatos, A. P. Colloidal nanocrystal synthesis and the organic–inorganic interface. *Nature* **437**, 664–670 (2005).
12. Burda, C., Chen, X., Narayanan, R. & El-Sayed, M. A. Chemistry and Properties of Nanocrystals of Different Shapes. *Chem Rev* **105**, 1025–1102 (2005).
13. Jun, Y., Choi, J. & Cheon, J. Shape Control of Semiconductor and Metal Oxide Nanocrystals through Nonhydrolytic Colloidal Routes. *Angewandte Chemie International Edition* **45**, 3414–3439 (2006).
14. Cozzoli, P. D., Pellegrino, T. & Manna, L. Synthesis, properties and perspectives of hybrid nanocrystal structures. *Chem Soc Rev* **35**, 1195 (2006).
15. Park, J., Joo, J., Kwon, S. G., Jang, Y. & Hyeon, T. Synthesis of Monodisperse Spherical Nanocrystals. *Angewandte Chemie International Edition* **46**, 4630–4660 (2007).
16. Fernández-García, M., Martínez-Arias, A., Hanson, J. C. & Rodriguez, J. A. Nanostructured Oxides in Chemistry: Characterization and Properties. *Chem Rev* **104**, 4063–4104 (2004).
17. Rodríguez, J. P., Brotons, L., Bustamante, J. & Seoane, J. The application of predictive modelling of species distribution to biodiversity conservation. *Divers Distrib* **13**, 243–251 (2007).
18. Niederberger, M. Nonaqueous Sol–Gel Routes to Metal Oxide Nanoparticles. *Acc Chem Res* **40**, 793–800 (2007).

19. Adler, S. B. Factors Governing Oxygen Reduction in Solid Oxide Fuel Cell Cathodes. *Chem Rev* **104**, 4791–4844 (2004).
20. Gur, I., Fromer, N. A., Geier, M. L. & Alivisatos, A. P. Air-Stable All-Inorganic Nanocrystal Solar Cells Processed from Solution. *Science (1979)* **310**, 462–465 (2005).
21. Palmisano, G., Augugliaro, V., Pagliaro, M. & Palmisano, L. Photocatalysis: a promising route for 21st century organic chemistry. *Chemical Communications* 3425 (2007) doi:10.1039/b700395c.
22. Reed, J. & Ceder, G. Role of Electronic Structure in the Susceptibility of Metastable Transition-Metal Oxide Structures to Transformation. *Chem Rev* **104**, 4513–4534 (2004).
23. Chiesa, M. *et al.* Excess Electrons Stabilized on Ionic Oxide Surfaces. *Acc Chem Res* **39**, 861–867 (2006).
24. Zhao, J., Li, B., Onda, K., Feng, M. & Petek, H. Solvated Electrons on Metal Oxide Surfaces. *Chem Rev* **106**, 4402–4427 (2006).
25. Osgood, R. Photoreaction Dynamics of Molecular Adsorbates on Semiconductor and Oxide Surfaces. *Chem Rev* **106**, 4379–4401 (2006).
26. Alivisatos, A. P. Perspectives on the Physical Chemistry of Semiconductor Nanocrystals. *J Phys Chem* **100**, 13226–13239 (1996).
27. El-Sayed, M. A. Small Is Different: Shape-, Size-, and Composition-Dependent Properties of Some Colloidal Semiconductor Nanocrystals. *Acc Chem Res* **37**, 326–333 (2004).
28. El-Sayed, M. A. Some Interesting Properties of Metals Confined in Time and Nanometer Space of Different Shapes. *Acc Chem Res* **34**, 257–264 (2001).
29. Ghosh, S. K. & Pal, T. Interparticle Coupling Effect on the Surface Plasmon Resonance of Gold Nanoparticles: From Theory to Applications. *Chem Rev* **107**, 4797–4862 (2007).
30. Narayanan, R. & El-Sayed, M. A. Effect of Catalysis on the Stability of Metallic Nanoparticles: Suzuki Reaction Catalyzed by PVP-Palladium Nanoparticles. *J Am Chem Soc* **125**, 8340–8347 (2003).
31. Narayanan, R. & El-Sayed, M. A. Changing Catalytic Activity during Colloidal Platinum Nanocatalysis Due to Shape Changes: Electron-Transfer Reaction. *J Am Chem Soc* **126**, 7194–7195 (2004).
32. Narayanan, R. & El-Sayed, M. A. Shape-Dependent Catalytic Activity of Platinum Nanoparticles in Colloidal Solution. *Nano Lett* **4**, 1343–1348 (2004).
33. Narayanan, R. & El-Sayed, M. A. Catalysis with Transition Metal Nanoparticles in Colloidal Solution: Nanoparticle Shape Dependence and Stability. *J Phys Chem B* **109**, 12663–12676 (2005).
34. Bratlie, K. M., Lee, H., Komvopoulos, K., Yang, P. & Somorjai, G. A. Platinum Nanoparticle Shape Effects on Benzene Hydrogenation Selectivity. *Nano Lett* **7**, 3097–3101 (2007).
35. Pankhurst, Q. A., Connolly, J., Jones, S. K. & Dobson, J. Applications of magnetic nanoparticles in biomedicine. *J Phys D Appl Phys* **36**, R167–R181 (2003).
36. Lu, A.-H., Salabas, E. L. & Schüth, F. Magnetic Nanoparticles: Synthesis, Protection, Functionalization, and Application. *Angewandte Chemie International Edition* **46**, 1222–1244 (2007).
37. Jun, Y., Choi, J. & Cheon, J. Heterostructured magnetic nanoparticles: their versatility and high performance capabilities. *Chem. Commun.* 1203–1214 (2007) doi:10.1039/B614735F.

38. Kwolek, P. *et al.* Photoelectrochemistry of n-type antimony sulfoiodide nanowires. *Nanotechnology* **26**, (2015).
39. Tamilselvan, M. & Bhattacharyya, A. J. Antimony sulphoiodide (SbSI), a narrow band-gap non-oxide ternary semiconductor with efficient photocatalytic activity. *RSC Adv* **6**, 105980–105987 (2016).
40. Nie, R. *et al.* Efficient Solar Cells Based on Light-Harvesting Antimony Sulfoiodide. *Adv Energy Mater* **8**, (2018).
41. Jung, K. W. & Choi, Y. C. Compositional Engineering of Antimony Chalcogenides via a Two-Step Solution Process for Solar Cell Applications. *ACS Appl Energy Mater* (2021) doi:10.1021/acsaem.1c02676.
42. Green, M. A. How Did Solar Cells Get So Cheap? *Joule* **3**, 631–633 (2019).
43. Green, M. A. Commercial progress and challenges for photovoltaics. *Nat Energy* **1**, 15015 (2016).
44. Green, M. A. & Bremner, S. P. Energy conversion approaches and materials for high-efficiency photovoltaics. *Nat Mater* **16**, 23–34 (2017).
45. Green, M. A. *et al.* Solar cell efficiency tables (Version 58). *Progress in Photovoltaics: Research and Applications* **29**, 657–667 (2021).
46. Kwolek, P., Oszejca, M. & Szaciłowski, K. Catecholate and 2,3-acenediolate complexes of d0 ions as prospective materials for molecular electronics and spintronics. *Coord Chem Rev* **256**, 1706–1731 (2012).
47. Gawęda, S. *et al.* Hybrid Semiconducting Materials: New Perspectives for Molecular-Scale Information Processing. in *Molecular and Supramolecular Information Processing* 121–173 (Wiley, 2012). doi:10.1002/9783527645442.ch7.
48. Rakovich, Y. P., Jäckel, F., Donegan, J. F. & Rogach, A. L. Semiconductor nanowires self-assembled from colloidal CdTe nanocrystal building blocks: optical properties and application perspectives. *J Mater Chem* **22**, 20831 (2012).
49. Zhong, H., Nagy, M., Jones, M. & Scholes, G. D. Electronic States and Exciton Fine Structure in Colloidal CdTe Nanocrystals. *The Journal of Physical Chemistry C* **113**, 10465–10470 (2009).
50. Akhavan, V. A. *et al.* Colloidal CIGS and CZTS nanocrystals: A precursor route to printed photovoltaics. *J Solid State Chem* **189**, 2–12 (2012).
51. Mousavi, S. H., Müller, T. S. & de Oliveira, P. W. Synthesis of colloidal nanoscaled copper–indium–gallium–selenide (CIGS) particles for photovoltaic applications. *J Colloid Interface Sci* **382**, 48–52 (2012).
52. Nakamura, M. *et al.* Cd-Free Cu(In,Ga)(Se,S)₂ Thin-Film Solar Cell With Record Efficiency of 23.35%. *IEEE J Photovolt* **9**, 1863–1867 (2019).
53. Suryawanshi, M. P. *et al.* CZTS based thin film solar cells: a status review. *Materials Technology* **28**, 98–109 (2013).
54. Zhou, H. *et al.* CZTS nanocrystals: a promising approach for next generation thin film photovoltaics. *Energy Environ Sci* **6**, 2822 (2013).
55. Ghorpade, U. *et al.* Towards environmentally benign approaches for the synthesis of CZTSSe nanocrystals by a hot injection method: a status review. *Chemical Communications* **50**, 11258 (2014).

56. Kumar, M., Dubey, A., Adhikari, N., Venkatesan, S. & Qiao, Q. Strategic review of secondary phases, defects and defect-complexes in kesterite CZTS–Se solar cells. *Energy Environ Sci* **8**, 3134–3159 (2015).
57. Pazos-Outón, L. M., Xiao, T. P. & Yablonovitch, E. Fundamental Efficiency Limit of Lead Iodide Perovskite Solar Cells. *J Phys Chem Lett* **9**, 1703–1711 (2018).
58. Snaith, H. J. Perovskites: The Emergence of a New Era for Low-Cost, High-Efficiency Solar Cells. *J Phys Chem Lett* **4**, 3623–3630 (2013).
59. Babayigit, A. *et al.* Assessing the toxicity of Pb- and Sn-based perovskite solar cells in model organism *Danio rerio*. *Sci Rep* **6**, 18721 (2016).
60. Babayigit, A., Ethirajan, A., Muller, M. & Conings, B. Toxicity of organometal halide perovskite solar cells. *Nat Mater* **15**, 247–251 (2016).
61. Rong, Y. *et al.* Challenges for commercializing perovskite solar cells. *Science (1979)* **361**, (2018).
62. Correa-Baena, J.-P. *et al.* Promises and challenges of perovskite solar cells. *Science (1979)* **358**, 739–744 (2017).
63. Savory, C. N., Walsh, A. & Scanlon, D. O. Can Pb-Free Halide Double Perovskites Support High-Efficiency Solar Cells? *ACS Energy Lett* **1**, 949–955 (2016).
64. Xiang, W. & Tress, W. Review on Recent Progress of All-Inorganic Metal Halide Perovskites and Solar Cells. *Advanced Materials* **31**, 1902851 (2019).
65. Saparov, B. *et al.* Thin-Film Deposition and Characterization of a Sn-Deficient Perovskite Derivative Cs_2SnI_6 . *Chemistry of Materials* **28**, 2315–2322 (2016).
66. Konstantakou, M. & Stergiopoulos, T. A critical review on tin halide perovskite solar cells. *J Mater Chem A Mater* **5**, 11518–11549 (2017).
67. Li, W. *et al.* Chemically diverse and multifunctional hybrid organic–inorganic perovskites. *Nat Rev Mater* **2**, 16099 (2017).
68. Li, M. *et al.* Advances in Tin(II)-Based Perovskite Solar Cells: From Material Physics to Device Performance. *Small Struct* **3**, 2100102 (2022).
69. Sun, N. *et al.* Architecture of p-i-n Sn-Based Perovskite Solar Cells: Characteristics, Advances, and Perspectives. *ACS Energy Lett* **6**, 2863–2875 (2021).
70. Yang, W., Igbari, F., Lou, Y., Wang, Z. & Liao, L. Tin Halide Perovskites: Progress and Challenges. *Adv Energy Mater* **10**, 1902584 (2020).
71. Ke, W., Stoumpos, C. C. & Kanatzidis, M. G. “Unleaded” Perovskites: Status Quo and Future Prospects of Tin-Based Perovskite Solar Cells. *Advanced Materials* **31**, 1803230 (2019).
72. Stoumpos, C. C. *et al.* Hybrid Germanium Iodide Perovskite Semiconductors: Active Lone Pairs, Structural Distortions, Direct and Indirect Energy Gaps, and Strong Nonlinear Optical Properties. *J Am Chem Soc* **137**, 6804–6819 (2015).
73. Ke, W. & Kanatzidis, M. G. Prospects for low-toxicity lead-free perovskite solar cells. *Nat Commun* **10**, 965 (2019).
74. Hu, H., Dong, B. & Zhang, W. Low-toxic metal halide perovskites: opportunities and future challenges. *J Mater Chem A Mater* **5**, 11436–11449 (2017).

75. Stoumpos, C. C., Malliakas, C. D. & Kanatzidis, M. G. Semiconducting Tin and Lead Iodide Perovskites with Organic Cations: Phase Transitions, High Mobilities, and Near-Infrared Photoluminescent Properties. *Inorg Chem* **52**, 9019–9038 (2013).
76. Stoumpos, C. C. *et al.* Hybrid Germanium Iodide Perovskite Semiconductors: Active Lone Pairs, Structural Distortions, Direct and Indirect Energy Gaps, and Strong Nonlinear Optical Properties. *J Am Chem Soc* **137**, 6804–6819 (2015).
77. Moritomo, Y. *et al.* Electronic structure of double-perovskite transition-metal oxides. *Phys Rev B* **61**, R7827–R7830 (2000).
78. Sun, Y.-Y., Agiorgousis, M. L., Zhang, P. & Zhang, S. Chalcogenide Perovskites for Photovoltaics. *Nano Lett* **15**, 581–585 (2015).
79. Niu, S. *et al.* Bandgap Control via Structural and Chemical Tuning of Transition Metal Perovskite Chalcogenides. *Advanced Materials* **29**, 1604733 (2017).
80. Tiwari, D., Hutter, O. S. & Longo, G. Chalcogenide perovskites for photovoltaics: current status and prospects. *Journal of Physics: Energy* **3**, 034010 (2021).
81. Yu, Z. *et al.* Transition metal-doped chalcogenide perovskite magnetic semiconductor $\text{B}_{1-x}\text{A}_x\text{Z}_y\text{S}_{3-y}$. *J Magn Magn Mater* **563**, 169886 (2022).
82. Stroyuk, O., Raevskaya, A. & Gaponik, N. Solar light harvesting with multinary metal chalcogenide nanocrystals. *Chem Soc Rev* **47**, 5354–5422 (2018).
83. Adjogri, S. J. & Meyer, E. L. Chalcogenide Perovskites and Perovskite-Based Chalcohalide as Photoabsorbers: A Study of Their Properties, and Potential Photovoltaic Applications. *Materials* **14**, 7857 (2021).
84. Kumar, M., Dubey, A., Adhikari, N., Venkatesan, S. & Qiao, Q. Strategic review of secondary phases, defects and defect-complexes in kesterite CZTS–Se solar cells. *Energy Environ Sci* **8**, 3134–3159 (2015).
85. Choi, Y. C. & Nie, R. Heavy pnictogen chalcohalides for efficient, stable, and environmentally friendly solar cell applications. *Nanotechnology* **34**, 142001 (2023).
86. Quarta, D. *et al.* Colloidal Bismuth Chalcohalide Nanocrystals. *Angewandte Chemie International Edition* **61**, (2022).
87. Sun, Y.-Y. *et al.* Discovering lead-free perovskite solar materials with a split-anion approach. *Nanoscale* **8**, 6284–6289 (2016).
88. Butler, K. T., Frost, J. M. & Walsh, A. Ferroelectric materials for solar energy conversion: photoferroics revisited. *Energy Environ Sci* **8**, 838–848 (2015).
89. Moroz, M. v. & Prokhorenko, M. v. Phase equilibria and thermodynamic properties of saturated solid solutions based on the compounds BiSeI, Bi₁₉Se₂₇I₃, and BiI₃ in the Ag–Bi–Se–I system. *Inorganic Materials* **52**, 765–769 (2016).
90. Ganesha, R., Arivuoli, D. & Ramasamy, P. Growth of some group V-VI-VII compounds from the vapour. *J Cryst Growth* **128**, 1081–1085 (1993).

91. Krauss, T. D. & Peterson, J. J. Electronic structure and optical transitions in colloidal semiconductor nanocrystals. in *Colloidal Quantum Dot Optoelectronics and Photovoltaics* 59–86 (Cambridge University Press, 2013). doi:10.1017/CBO9781139022750.004.
92. Jortner, J., Ratner, M. A., Ratner, M. A. & Jortner, J. *Molecular electronics*. (Blackwell Science Oxford, 1997).
93. Nobile, C. & Cozzoli, P. D. Synthetic Approaches to Colloidal Nanocrystal Heterostructures Based on Metal and Metal-Oxide Materials. *Nanomaterials* **12**, 1729 (2022).
94. Manna, L., Scher, E. C. & Alivisatos, A. P. Synthesis of Soluble and Processable Rod-, Arrow-, Teardrop-, and Tetrapod-Shaped CdSe Nanocrystals. *J Am Chem Soc* **122**, 12700–12706 (2000).
95. Ostwald, W. Über die vermeintliche Isomerie des roten und gelben Quecksilberoxyds und die Oberflächenspannung fester Körper. *Zeitschrift für Physikalische Chemie* **34U**, 495–503 (1900).
96. Hines, M. A. & Scholes, G. D. Colloidal PbS Nanocrystals with Size-Tunable Near-Infrared Emission: Observation of Post-Synthesis Self-Narrowing of the Particle Size Distribution. *Advanced Materials* **15**, 1844–1849 (2003).
97. Owen, J. The coordination chemistry of nanocrystal surfaces. *Science (1979)* **347**, 615–616 (2015).
98. Quarta, D. *et al.* Stable Ligand Coordination at the Surface of Colloidal CsPbBr₃ Nanocrystals. *J Phys Chem Lett* **10**, 3715–3726 (2019).
99. Wang, Z. L. Transmission Electron Microscopy of Shape-Controlled Nanocrystals and Their Assemblies. *J Phys Chem B* **104**, 1153–1175 (2000).
100. Ben, T., Allah, R. F., Sales, D. L., González, D. & Molina, S. I. Transmission Electron Microscopy of 1D-Nanostructures. in *Transmission Electron Microscopy Characterization of Nanomaterials* 657–701 (Springer Berlin Heidelberg, 2014). doi:10.1007/978-3-642-38934-4_14.
101. Debellis, D., Gigli, G., ten Brinck, S., Infante, I. & Giansante, C. Quantum-Confined and Enhanced Optical Absorption of Colloidal PbS Quantum Dots at Wavelengths with Expected Bulk Behavior. *Nano Lett* **17**, 1248–1254 (2017).
102. Hens, Z. & Martins, J. C. A Solution NMR Toolbox for Characterizing the Surface Chemistry of Colloidal Nanocrystals. *Chemistry of Materials* **25**, 1211–1221 (2013).
103. Moreels, I. *et al.* Composition and Size-Dependent Extinction Coefficient of Colloidal PbSe Quantum Dots. *Chemistry of Materials* **19**, 6101–6106 (2007).
104. Quarta, D. *et al.* Colloidal Bismuth Chalcogenide Nanocrystals. *Angewandte Chemie International Edition* **61**, (2022).
105. Balakrishnan, S. K., Parambil, P. C. & Edri, E. Mechanistic Insight into the Topotactic Transformation of Trichalcogenides to Chalcogenides. *Chemistry of Materials* **34**, 3468–3478 (2022).
106. Leo Lehrman, B. *3 Vortmann and Metzl. Currie: J. Phys. Chem* vol. 44 <https://pubs.acs.org/sharingguidelines> (1905).
107. Ghorpade, U. V. *et al.* Emerging Chalcogenide Materials for Energy Applications. *Chem Rev* **123**, 327–378 (2023).